Breathing Mode Effects on Hall Thruster Plasma Quantities and Channel Wall Power Loss

Nadiah Jenkins

A thesis
submitted in partial fulfillment of the
requirements for the degree of

Master of Science in Aeronautics and Astronautics

University of Washington

2019

Committee:

Justin Little, Chair

Jeffery Monheiser

Program Authorized to Offer Degree:
Aeronautics and Astronautics

University of Washington

Abstract

Breathing Mode Effects on Hall Thruster Plasma Quantities and Channel Wall Power Loss

Nadiah Jenkins

Chair of the Supervisory Committee:
Justin Little
Department of Aeronautics and Astronautics

Breathing mode instabilities, axially-oriented waves between $5 - 40$ kHz, have been observed in Hall thruster operation since the earliest days of experimental research, including their ability to grow large enough to extinguish the working plasma. Recent forays into higher power Hall thrusters and extended mission durations highlight the need to understand the mechanisms and consequences of the breathing mode. While experiments in the last 20 years have increased the understanding of the time dependent behavior of plasma within the channel, analytical and numerical models have struggled to accurately replicate the oscillation or predict its effects.

This thesis presents a partial-D fluid model to numerically solve for plasma and neutral density, ion and electron velocity, and mass utilization in a radially- and azimuthally-symmetric SPT-type Hall thruster. After an ideal steady state solution converges, these quantities evolve in the presence of a driven sinusoidal oscillation of the electric field, which simulates a breathing mode oscillation. Separate simulations vary the frequency and amplitude of the driven oscillations to test spatial and temporal variations of the acceleration region. Then, analysis focuses on how the oscillations affect plasma quantities and key contributors to channel wall power loss. This work provides clarification on how the breathing mode perturbs the plasma and how this compares with experiments in the literature.

TABLE OF CONTENTS

LIST OF FIGURES

ACKNOWLEDGMENTS

Thank you to my partner, Chris, for providing such steadfast support through every stage of my graduate school career. With your help I realized I could, in fact, pursue my dreams, then you moved with me to Seattle and supported me through every frustration and stumbling block along the way. This degree would not have been possible without you.

This thesis would also not have seen the light of day without the guidance and support of my adviser, Justin Little. Through vague gestures and ideas, you managed to figure out where I wanted to go with a thesis, and ensured I didn't get lost along the way.

My colleagues in SPACE Lab — Charlie Kelly, Diego Mejia Montaño, Curtis Promislow, Anna Sheppard, Peter Thoreau — provided me with one of the best working environments I've had the privilege of experiencing, marked by their wit, generosity, and insight. Other fellow women in aeorspace, Ellie Forbes and Aria Johansen, also gave me incredible amounts of academic and emotional support that I will be eternally grateful for. I was ready for graduate school to be a cutthroat academic nightmare, but you all showed me the importance of compassion and community. Thank you.

Finally, I couldn't have taken the million and one steps necessary to get this far in my education without inspiration from my sisters-from-another-mother: Amy, Jess, Kori, Kae-Lin, and Lisa. You've guided me through more maelstroms than I can count.

DEDICATION

to my mother, Kamariah,

who always knew I could

Chapter 1
INTRODUCTION

1.1 Electric Propulsion and Hall Thrusters

The theoretical origins of electric propulsion can be traced back to the early years of the twentieth century. Konstantin Eduardovitch Tsiolkovsky, better known for his classical rocket equation, postulated the idea of electricity ejecting particles from a rocket at high velocities [34]. Kondratyuk These musings by Tsiolkovsky, Goddard, and others, continued through the 1910s and 1920s, briefly punctuated by the creation of the first electrothermal thruster by Glushko [7]. Unfortunately for the field, the years leading up to and through World War II focused rocket science research on chemical rockets and chemical fuels, stagnating EP research until after the war.

It was the rising prominence of nuclear science, and the idea of a nuclear fission-powered rocket, that eventually rekindled interest in electric propulsion. According to initial designs, nuclear rockets would produce thrust through thermal processes. However, early on scientists realized that this would require the use of exotic materials and advanced reactor designs that they simply did not have; those designs would have to wait for a more distant future. By contrast, switching from a thermal scheme to an electric one made these alternative rocket designs more feasible [7].

Electric propulsion also owes its eventual growth to the ion beam and beam neutralization research through the 1940s and 1950s; without a reliable and strong source of ions, experimental EP would have never been feasible in the first place. In particular, the Kaufman ion source, developed by Harold Kaufman at NASA Lewis (Glenn) Research center, provided a reliable ion source. This ion source heavily contributed to the initial design of the gridded ion thruster, eventually informing the next fifty years of ion thruster at NASA [23].

Finally, one could argue that development of electric propulsion systems languished because of initial, unreasonable expectations from the field itself. Choueiri notes that many of the early pioneers of aerospace engineering were captivated by turn-of-the-century science fiction that emphasized human exploration, which requires power schemes that, even now, are unreasonable. It was only when the realm of expectations was shifted - from human spaceflight to telecommunications - that experimental research in electric propulsion thrusters was able to take off [7].

Hall-effect thruster (hereafter simply called "Hall thruster") designs emerged in the 1950s, with a majority of the early research coming from the Soviet Union (NASA decided to focus on gridded ion thrusters due to their higher efficiency). Within the USSR, multiple agencies contributed to Hall thruster research, which also led to different preferred designs. Most prominently, OKB-Fakel supported research in the stationary plasma thruster (SPT) and the Tsentral Institute of Machinebuilding focused on the alternative, the thruster with anode layer (TAL) design. As the prevailing design coming out of the 1990s has been the SPT, this thesis focuses on that design, especially its insulating walls with high secondary electron emission (relative to a conductive channel wall) [25].

Through the 1970s and 1980s, research continued along both design lineages. In 1971, the first flight-capable Hall thruster (an SPT) was flown aboard the weather satellite *Meteor*. [28] G.N. Tilinin and others investigated operating instabilities. [33] Towards the mid-1970s, as lifetime data started to accumulate, erosion became a concern as well [25].

Following the fall of the Soviet Union in the early 1990s, NASA began to investigate Hall thrusters more closely, especially the newly-accessible Russian SPTs [30]. At first, U.S. spacecraft and satellite manufacturers continued to use Hall thrusters manufactured by Fakel, a Russian company. Fakel-produced thrusters were used on American spacecraft until 2006, when Busek, Inc. (based in Boston, MA) was able to supply the Air Force TacSat-2 spacecraft with the 200-W BHT-200 thruster. [16] More recently, Aerojet Rocketdyne successfully flight-tested their 5-kW XR-5 Hall thruster in 2010 on Lockheed Martin's AEHF-1 satellite. Building on this system architecture, the 12-kW X-12 model is currently in development [36].

The commercial and research applications for Hall thrusters have also expanded since the the early 2000s. Within NASA's future plans, the Pysche mission to explore an iron-nickel asteroid and the Advanced Electric Propulsion System (AEPS) for the NASA Gateway will both use Hall thrusters, either in singular or combination. Additionally, NASA has invested in the development of both low- and high-power Hall thrusters, ranging from the sub-kilowatt thrusters at JPL [8] to the 100+ kW thruster being jointly researched by the University of Michigan and Aerojet Rocketdyne [32].

1.2 Thesis Motivation

Both current and future uses of Hall thrusters in space rely on thruster longevity over time and usage. As stated previously, early implementation of Hall thruster technology struggled with lifetime prediction, which resulted in early flight losses[25]. While present research has the benefit of actual data on thruster lifetimes, the need to extend those limits persists with the desire to us Hall thrusters for longer, interplanetary missions.

Critically, the source of thruster failure can be traced back to the operating plasma itself, since the system lacks any mechanical devices and few electrical interfaces that could fail. To those familiar with experimental plasma physics, this comes as little surprise, given the fickle nature of plasma and the sheer number of factors that can start, maintain, or extinguish a plasma. Two inexplicable behaviors can arise during the operation of a Hall thruster: etching of the ceramic insulator lining the thruster channel, and periodic, axially-oriented fluctuations in the plasma and neutral density fluctuations — the "breathing mode." This thesis seeks to link these two non-ideal behaviors by analyzing the effect a breathing mode oscillation would have on the interactions between the operating plasma and the thruster walls.

Using a numerical solver within Wolfram's Mathematica software, a non-dimensionalized two-fluid equation for the cold plasma within a Hall thruster is used to simulate plasma quantities of neutral density, ion velocity, electron velocity, and mass (propellant) utilization. These four quantities are resolved in space and time along the axial direction of the

thruster, assuming a one-dimensional system that is radially and azimuthally symmetric. These quantities are then used to derive localized heat flux and spatially-averaged power loss to the channel walls. The Mathematica model converges on a solution in all cases within a short ($\leq$ 30 min) time frame, with results that are physically reasonable compared to expected Hall thruster behavior.

Once steady state results are found, a sinusoidal driven oscillation is applied to the electric field location in order to simulate the breathing mode. In one simulation set, the location of the peak electric field is axially displaced between 0.0001 m and 0.005 m, which produces instantaneous power losses to the wall of over 50% of the total input power. In another simulation set, the frequency of the oscillation is varied from 1 kHz to 50 kHz, mimicking the literature range for breathing mode, and only produces a maximum instantaneous power loss of 36% of the total input power. Between the two variation sets, axial displacement exhibits a stronger influence on both plasma parameter ranges and power loss ranges, as well as producing non-sinusoidal behavior that is not replicated in the frequency variation case. From these observations, axial movement of the acceleration region is likely to be a contributing factor to breathing mode oscillations, though the cause of the displacement remains unknown.

Chapter 2

BACKGROUND

2.1 Hall Thruster Basic Plasma Physics

While there are multiple variations for Hall thruster configuration, this thesis assumes that the thruster model is a stationary-plasma type (SPT) thruster, as illustrated in Fig. 2.1. For this configuration, the electric field orients axially through the channel, and the magnetic field sits radially (orthogonal to the electric field). The channel walls are also made of some insulating material (e.g. boron nitride ceramics) and do not conduct.

Hall thrusters take advantage of the eponymous Hall effect, a phenomenon where charged species moving through a medium in a magnetic field deviate from their original straight line path due to the Lorentz force, which concentrates charged species on one side of the medium and induces an electric field that is oriented to resist further charge separation. In the case of the Hall thruster, this effect creates an azimuthal current of electrons at the exit plane of the thruster, which in turn bolsters the axial electric field that accelerates ions along the channel length.

Typically, at the base of the channel is an anode with a positive electric potential. At the exit plane of the channel, either at the center of the annulus (internally mounted) or, in the case of Fig. 2.1, fixed outside the circumference (externally mounted), is the hollow cathode, usually set to the ground potential of the greater spacecraft. To prevent the exhaust plasma from being attracted back to the spacecraft because of the differing potential between the spacecraft and the plasma, the hollow cathode discharges a steady current of electrons into the ion plume, neutralizing the plasma which continues onward through space at the exhaust velocity.

Electrons produced from this hollow cathode are also attracted into the Hall thruster by

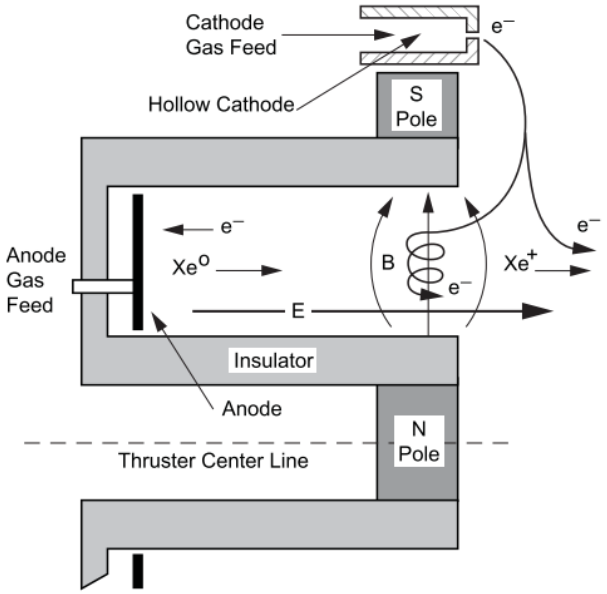

Figure 2.1: A cross section of a Hall thruster with the directions of the electric and magnetic fields and the ideal paths of the ions and electrons [16].

the anode. However, as mentioned earlier, many electrons are "caught" on the magnetic field due to their small mass and therefore small gyroradii (Larmor radii). This concentration of electrons towards the exit plane of the thruster accentuates the axial electric field. Due to the interaction with the radial magnetic field and the resulting Hall effect, the radii of both the electrons and the ions are used as minimum and maximum restraints, respectively, on the length of the channel, L. A Hall thruster channel must be sufficiently long enough to allow trapping of the electrons, but also short enough not to allow trapping of the ions in the same manner.

Assuming that the velocity of the electrons, $v_\perp$ is the thermal velocity, the gyroradius of either the ion or the electron can be defined in Eqn. 2.1, where m is the mass of the electron or ion, e is the elemental charge (multiplied by some constant if a non-singularly ionized species is used), and B is the magnitude of the magnetic field [16]. The channel length must

be much greater than $r_{L,electron}$ and much smaller than $r_{L,ion}$ simultaneously.

$$r_L = \frac{mv_\perp}{eB} = \frac{m}{eB}\sqrt{\frac{8eT_{eV}}{\pi m}} \tag{2.1}$$

Neutral gas, typically xenon, is injected into the channel near the anode. Neutral atoms and electrons in the region collide, leading to the production of ions. In this "ionization region" the majority of the ionization occurs due to charge-exchange and collisions between the neutrals and, as the neutrals draw closer to the end of the channel, electron-neutral collisions. This next region is then called the "acceleration region," where the electric field is near or at its maximum value, producing a sharp potential drop that accelerates ions to their exit velocity. When the ions leave the annulus at their exit velocity, they create thrust for the spacecraft. During operation, the high density of exiting ions create a plasma cloud, often called a "plume."

Idealized pictures of Hall thrusters place the maximum electric field at the exit plane of the thruster, aligning with the maximum magnetic field, as described in Fig. 2.2a. Experimental measurements of the axial electric field show that this is not necessarily the case, and that the peak electric field, and therefore the center of the acceleration region, may lie closer to the axial center of the thruster (Fig 2.2b) [2].

2.2 Breathing Mode Oscillations

Plasma systems experience a wide range of oscillations due to the large number of variables in the plasma "circuit" - including but not limited to the applied voltage, spatial currents, and particle densities. The types of oscillations along with their relevant operating regimes and amplitudes are summarized well in the review paper by Choueiri [6]. Of particular interest are the oscillations within the $1-20kHz$ band. Current models describe this oscillation band as resulting from a neutral density being depleted then replenished and again depleted near the exit plane of the thruster. This fluctuation was termed a "breathing" mode by Boeuf and Garrigues [3]. The amplitude of the breathing mode oscillation can each scales on par with the applied discharge voltage, which may extinguish the discharge altogether. Due to

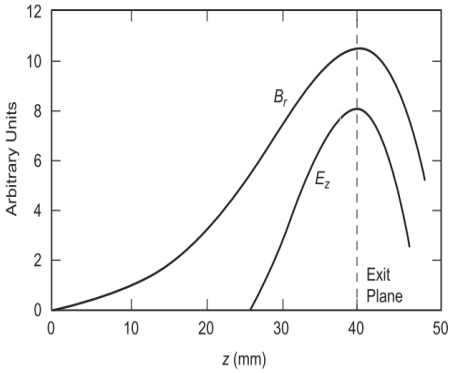

Idealized electric field distribution, where the peak value occurs at the exit plane. [16]

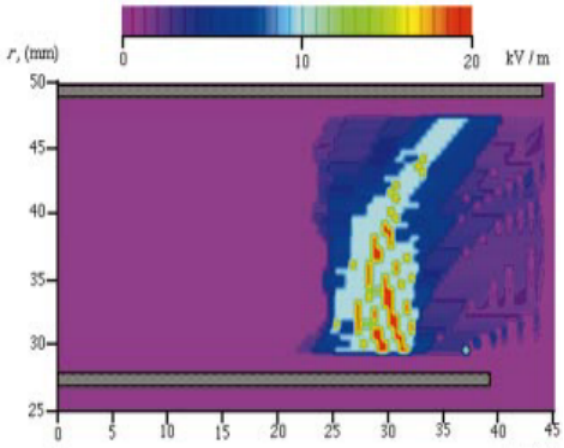

Experimental measurements of the axial electric field taken from an SPT thruster, where the x-axis measures the location along the channel length (mm). Note that the peak value of the electric field does *not* align with the exit plane of the thruster (approximately 40 mm) [6].

Figure 2.3: Comparison of the idealized and experimental locations of the maximum electric field along the axis of the thruster.

this destructive capability, this thesis will focus on the breathing mode oscillations only.

Breathing mode oscillations during Hall thruster experiments were reported as early as 1977 by Tilinin [33] during his study of the effect of high-frequency waves on Hall thruster operation. As the magnetic field in the channel varied relative to the calculated "ideal maximum magnetic field of the exit plane," clusters of frequencies would grow or decay. One such cluster in the 1-20 kHz range experienced two peaks across the magnetic field range, and reached voltages on par with the discharge voltage of the thruster.

During the late 1990s, the popular zero-dimensional "predator-prey" model was proposed by Fife et al. [13]. This model uses two partial differential equations to describe the time-dependent evolution of ion and neural species, which are similar to the Lokta-Volterra equations of biological systems. From the predator-prey model, Barral and Ahedo proposed a low-frequency model, a one-dimensional approach to describing small perturbation modes.

These models and their impact on this thesis are elaborated on in Chapter 3.

Empirically-informed studies of erosion have been with mixed success [15], and many other models have arisen to try to describe the breathing mode oscillations, both analytically [27] and numerically [24]. Others, like Romadanov et al., have tried to replicate the signal by forcing an oscillation through anode voltage in a cylindrical hall thruster (CHT). Ion velocity and density increased according to their forced oscillation, and the authors remark on the decreasing phase shift between the two quantities leading to an overall increase in discharge oscillation amplitudes. In this case, the oscillation also improves thruster performance (propellant utilization) [31].

2.3 Acceleration Region Interactions and Experimental Background

The acceleration region is often defined as the section of the channel thruster where the potential falls sharply, leading to rapid "acceleration" of ions from this point towards the channel exit. This potential drop also heats incoming electrons; therefore, the acceleration region also has the highest electron temperature of anywhere in the channel [19].

Laser-induced fluorescence (LIF) remains a popular method to study ion interactions within the channel of Hall thrusters. Not only is the technique non-intrusive for the operating Hall thruster under test, but it provides high-resolution spatial information about the ions and neutrals within the thruster channel. From this, species velocities can be calculated, and the changes in those velocities can provide insight into the mechanisms of oscillations such as the breathing mode.

Published research is scarce concerning the effect of the acceleration region on the presence, amplitude, or frequency of the breathing mode oscillation. In an effort to link acceleration region dynamics to the breathing mode, Dale et al. have used time-resolved LIF (TR-LIF) to analyze the anomalous electron transport that may contribute to breathing mode. They report that this transport varies over the cycle time, emphasizing the importance of a time-dependent model [11].

Young et al. show not only the typical ion velocity distribution functions, but also the

evolution of the electric field over a breathing mode cycle. Within the channel, the electric field oscillates in both axial location and in magnitude, with the field being more concentrated at the beginning of the cycle [37].

Other prominent papers focus on either fundamental understanding of the acceleration region or the influence of potential, magnetic field, and facility pressures on the acceleration region. In the former category, Vaudolon et al. studied the time-evolution of the electric field both in and outside the thruster channel. In their experiment, the external field varied more than the internal electric field, which showed only tiny variations in magnitude [35].

One well-studied phenomenon analyzed through LIF has been the effect of plasma potential magnitude on the location of the acceleration zone. Though several articles have looked at this experiment, consensus on the effect remains elusive. Hargus et al. concluded that, for their sub-kW laboratory Hall thruster, the width of the acceleration region remains unchanged [22]. However, Mazouffre et al. with the 5-kW PPSX000 Hall thruster [26] and Gawron et al. with the 1.5-kW PPS100-LM Hall thruster [14] describe the acceleration region narrowing with increased potential. By contrast, Chaplin et al., conducting experiments on JPL's 12.5-kW HERMeS thruster, describe a *broadening* of the acceleration region with increased potential [5]. As of this publishing, research thus far remains inconclusive.

A more consistent phenomenon affecting the acceleration region is the change with varying magnetic field strength. Many of the studies mentioned above show that with increased field strength, the acceleration zone moves further upstream into the thruster [14] [26].

Facility pressure has also been shown to affect the location of the acceleration region. Cusson et al., using LIF, saw the acceleration region move inward (away from the exit plane) due to both increasing facility background pressure and increased neutral flow from the cathode relative to the anode flow (flow fraction) [9].

Results gathered from LIF experiments have been used to inform analytical and numerical models of the acceleration region, including the size and location of the acceleration region within the thruster. The most symbiotic of these studies has been the work down by Jorns, who has published both experimental and computational models of the ionization region of

the thruster. The computational side of his work with Dale is expanded on in Chapter 3.

Overall, the dynamics of the acceleration mode, especially under a breathing mode oscillation, remains difficult to model accurately due to incomplete understanding of the physics involved. What stands out amongst nearly all the papers is the importance of a time-dependent model to preserve the oscillation effects on the plasma.

Chapter 3
ANALYTICAL MODELS

3.1 Prior Work and Models

Fife et al. presented the first comprehensive model for breathing mode oscillations that were comparable to experimental results [13]. This model is based on the predator-prey, or Lotka-Volterra, model, where a rough metaphor can be made that the ions are the "predator" of the system and the neutrals are the "prey" being consumed (ionized). Work by Boeuf and Garrigues expanded on this dynamic, showing the oscillation in system from fast ionization and neutral depletion to ionization collapse and neutral replenishment [3].

In their 2009 paper , Barral and Ahedo present a model for breathing mode oscillations which remain steady for the ratio of electron density over current, as well as the growth rate of current. The key objective for the paper was to reduce the time-dependence of the predator-prey model by Fife, as well as to expand the model from zero to one dimensionality [1]. In a thorough walkthrough, Barral starts with the usual time-dependent, two-fluid differential equations and Ohm's law, then starts to apply assumptions to chip away at the time dependence. Towards the final stroke to eliminate the time derivatives of the fluid equations, Barral states that the steady state solution relies not on the current or ion density separately. In fact, the only steady, well-defined solution exists for the *ratio* of density over current (n/I). Therefore, the spatial PDE system must be divided by current in order to be a satisfactory, quasisteady solution. The Barral model matches experimental evidence well at small perturbations, but does not accurately reproduce the breathing mode frequencies periodically [1].

The perturbation analysis given by Hara et al. in 2014 [21] presents a volume-averaged, two fluid model for Hall thrusters, comprised of ion and neutral continuity, momentum,

and electron energy equation. This blend of heavy species (ion and neutral) transport with perturbations in electron energy illustrates a system wherein the breathing mode originates from oscillations in electron energy. Hara et al. elect, like Barral and Ahedo, to work around the issue of "ionization length" in their model for breathing mode oscillations. A common conundrum in modeling Hall thruster physics, the ionization length would ideally describe the section of the thruster where the bulk of ionization happens, before the acceleration region depletes the plasma density. In models seeking to replicate the breathing mode, the ionization length is commonly targeted as the source of the oscillation: its contraction and growth could explain the oscillating densities further downstream at the exit plane. However, unlike a gridded ion thruster, the structure of the Hall thruster does not allow for clear delineation of where ionization starts or stops [16].

Rather than defining the ionization length through a combination of scaling law approximations as described by Goebel and previous literature [16], Hara et al. define ionization length as a function of channel length and width, ion acoustic speed, and mean ion velocity [21]. This approach links the ionization length more tightly to the the actual geometry of the thruster and the state of the plasma at a particular point in time - which also allows for time-dependent changes in the ionization length, as tackled in later models. In contrast to the model at the focus of this thesis, the paper also assume that the electric field and the electron velocity terms are constant.

A key feature of the 2014 Hara paper is the claim that the breathing mode is intimately tied to an "electron energy relaxation frequency." Restricting the model to only the continuity and momentum equations limited the system to damped oscillations only; introducing the electron energy, and perturbations therein, led to undamped oscillations. This relaxation frequency takes into account "electron convective heat flux, wall heat flux, and inelastic collisions," in line with the model's objective of capturing (previously neglected) transport processes related to the breathing mode [21].

Working from the Hara et al. 2014 model, in 2017 Dale et al. sought to take the volume-averaged, two-fluid model and implement perturbations across the electron temperature,

electric field, and one new conceptual quantity: the ionization *region* length [10]. The overarching model described in the paper postulates that there are actually three regions along the Hall thruster channel: a neutral region, an ionization region, and the acceleration region. The boundary between the neutral and ionization region, described as an "ionization front," fluctuates with time to produce a breathing mode. Much like the 2014 Hara et al. paper, oscillations remained damped with all subsets of the model's equations until the electric field was changed from a constant function to a function of electron velocity and total collision rate, and therefore, time-dependent.

A time-dependent electric field played a pivotal role in the model published in 2018, again by Hara, who proposed an electron pressure coupling scheme. First, the electric field is defined through a cross-field electron transport equation, which includes electron pressure and the cross-field electron mobility term. Then, this equation is folded into the ion momentum equation to incorporate the pressure and mobility terms with the ion velocities and densities. Coupling reduces the numerical oscillations that can arise in these fluid models [20].

The fluid equations presented in the 2018 Hara paper inform the fluid model used in this thesis. The wall loss formulation also served as basis for this thesis's assessment of power loss, in partnership with a mutual source, Goebel's 2008 textbook [16].

3.2 Proposed Fluid Model for Analysis

The analysis in this thesis is primarily based on the 1D fluid models proposed by both Dale [10] and Hara [20]. Both are radially and azimuthally symmetric; this is sufficient for the study of a breathing mode-like oscillation, since this has only been observed oscillating in the axial direction [37].

The model in this thesis starts from the following equations: ion continuity (Eqn. 3.2), neutral continuity (Eqn. 3.6), ion momentum (Eqn. 3.9), and charge conservation (Eqn. 3.10).

3.2.1 Thruster Geometry

The test thruster for this model uses a nominal voltage of 300V, a discharge current of 4.5 A, and mass flow rate of $5.4mg/s$ based on the SPT-100 performance numbers commonly cited in Hall thruster literature [29]. The channel has an outer radius of 5 cm, an inner radius of 3.45 cm, and a length (depth) of 7 cm, also based on the SPT-100 geometry. In addition, scaling laws give a range for optimum current densities is 0.1 to 0.15 A/cm^2; these dimensions approximate the current density at 0.11, which falls within the given range (Eqn. 3.1) [16].

$$j_{typical} = \frac{I_d}{A_{an}} = 0.11 \frac{\text{A}}{\text{cm}^2} \tag{3.1}$$

Along a non-dimensionalized thruster length $\hat{z}$, where the exit plane is located at $\hat{z} = 1$, the nominal acceleration region centers at $\hat{z} = 0.64$, hereafter known as $\hat{z}_a$, with a width of 0.02. The minimum electron temperature of the plasma (i.e. near the anode) is assumed to be $2.5eV$, while the maximum temperature is $30eV$, approximately one-tenth of the discharge voltage per design rule of thumb [16] [6].

3.2.2 Ion Continuity

The ion continuity equation relates the variation of the ion density (n_i) across both time and the axial variation in momentum (calculated with the ion velocity, u_i) to the generation of ions through the channel. This source term on the right hand side is the product of the ion density and the ionization frequency, $\dot{n}_{ion}$ (Eqn. 3.2).

$$\frac{\partial n_i}{\partial t} + \frac{\partial}{\partial z}(n_i u_{i,z}) = n_i \dot{n}_{ion} \tag{3.2}$$

The ionization frequency is further defined in terms of the neutral density (n_n) and the ionization rate (R_{ion}), as seen in Eqn. 3.3.

$$\dot{n}_{ion} = n_n R_{ion} \tag{3.3}$$

This leads to the expanded form of ion continuity used for numerical modeling, Eqn. 3.4.

$$\frac{\partial n_i}{\partial t} + \frac{\partial}{\partial z}(n_i u_{i,z}) = n_i n_n R_{ion} \tag{3.4}$$

The ionization rate is often determined to be a function of temperature that is fitted to previous tabulated (experimental) data of cross sections and excitation rates, and this model takes the same approach. Goebel offers both the tabulated data and ionization rate equations for two regimes: greater and less than 5 eV. Since this thesis will examine the effects of a dynamic acceleration zone where temperatures are over 5 eV, only one equation will be used, as defined in Eqn. 3.5 [16].

$$R_{ion}(T_{eV}) = 10^{-20}[(3.97 + 0.643T_{eV} - 0.0368T_{eV}^2)\exp\left(\frac{-12.127}{T_{eV}}\right)]\sqrt{\frac{8eT_{eV}}{\pi m_e}} \tag{3.5}$$

This equation for ion continuity also ignores the ion loss due to plume expansion, which is addressed in the Hara 1D model [20]. As stated in the paper, the system is much more sensitive to changing conditions within the thruster, while the plume loss occurs outside the thruster, past the exit plane. Therefore, to keep this model concise, the plume-related losses will be ignored.

3.2.3 Neutral Continuity

The neutral continuity equation, Eqn. 3.6, relates the time and spatial change in the neutral density (n_n) to the neutral velocity (u_n) and the depletion of neutrals through ionization ($\dot{n}_{ion}$). This equation uses the same $\dot{n}_{ion}$ term defined above in Eqn. 3.3; however, because the neutrals are being consumed during the ionization process, the source term is negative. The ionization rate is also defined through the same fitted function from Goebel as seen in Eqn. 3.5 [16].

$$\frac{\partial n_n}{\partial t} + \frac{\partial}{\partial z}(n_n u_{n,z}) = -\dot{n}_{ion} \tag{3.6}$$

Unlike in the case for the ions where the velocity of the ions is changing due to an ever-present electric field, this model assumes that the velocity of the neutrals stays constant at the feed velocity. In this model, the feed velocity for the neutral gas is defined to be the thermal velocity (Eqn. 3.7) at room temperature, where $T = 298$ K, and $m_i = 2.1 \times 10^{-25}$ kg, and k_B is Boltzmann's constant.

$$u_n = \sqrt{\frac{k_B T_{room}}{m_i}} \tag{3.7}$$

Expanding the model like the ion continuity - including the definitions of the ionization frequency - yields the expanded form of the neutral continuity the computational model, Eqn. 3.8. Like the ion continuity, the neutral continuity equation (Eqn. 3.6) does not take into account plume expansion losses because of their proportionally lower impact on the system.

$$\frac{\partial n_n}{\partial t} + \frac{\partial}{\partial z}(n_n u_{n,z}) = -n_i n_n R_{ion} \tag{3.8}$$

3.2.4 Ion Momentum

The ion momentum equation relates the change in momentum over both time and space for the ions to the electric field (also a function of space and time) and the ionization rate. Neutrals that undergo ionization do not suddenly lose their momentum, but rather, their momentum is now counted towards the entirety of the ion-fluid's momentum.

$$\frac{\partial}{\partial t}(n_i u_{i,z}) + \frac{\partial}{\partial z}(n_i u_{i,z}^2) = \frac{e}{m_i} n_i E_z + n_i n_n R_{ion} u_n \tag{3.9}$$

3.2.5 Charge Conservation

Quasi-neutrality of the plasma is preserved within the Hall thruster plasma because the Debye length is, at the most, within the order of 10^{-5} m; this is at least an order of magnitude smaller than any spatial specification in the system. This property of quasineutrality can

be used to relate the ion and electron velocity and densities, illustrated through charge conservation, Eqn. 3.10.

The charge conservation equation says that the positive charge change across the spatial dimension, calculated through the ion velocity, density, and the elemental charge (e), has to be equal to the change in the negative charge, calculated through the electron density (n_e), electron velocity (u_e), and the elemental charge.

$$\nabla \cdot (en_i\vec{u_i} - en_e\vec{u_e}) = 0 \tag{3.10}$$

Quasineutrality also allows the assumption that the ion density is equal to the electron density. These are both then referred to as "plasma density," or n_p. The equation then used in the model is Eqn. 3.11.

$$\frac{\partial}{\partial z}(n_p u_i) = \frac{\partial}{\partial z}(n_p u_e) \tag{3.11}$$

3.2.6 Electric Field and Temperature Assumptions

Based on experimental data, the electric field was assumed to take a Gaussian shape with its peak at the center of a prescribed acceleration [6]. The work by Young et al. shows this distribution most recently [37]. This Gaussian shape is described in Eqn. 3.12, where V_{dt} is the assigned discharge voltage, $\delta(t)$ alters the width of the Gaussian function, z is the distance along the channel where $z = 0$ is the anode, and z_a is the assigned peak of the electric field.

$$E_{steady} = \frac{V_d}{\sqrt{2\pi\delta^2}} \exp\left(-\frac{(z - z_a)^2}{2\delta^2}\right) \tag{3.12}$$

This non-time-dependent function assumes that the electric field shape does not change in either shape or magnitude with any of the parameters under study (e.g. density, electron velocity). By extension, this also assumes that the electrons involved in the azimuthal Hall current at the exit plane of the thruster are also unaffected by the changing parameters.

Lastly, there is no equation in this model that keeps the potential of the system self-consistent with the defined discharge voltage, V_d.

The temperature (Eqn. 3.13) is assumed to follow the shape of the electric field via an assumed background electron temperature, T_0 (eV), and a maximum background electron temperature, T_m (eV). This produces a Gaussian shape, much like the electric field, which is also based on experimental observation [2]. This close relationship between electric field and temperature both follows experimental data [6] and physical explanations: the growing electric field would be due to an increased density in the azimuthal, Hall current electrons, which would lead to more interactions with the neutral and ion species flying by, and such interactions would lead to more Ohmic heating and therefore a higher temperature [16].

$$T_{steady} = (T_m - T_0)\exp\left(-\frac{(z - z_a)^2}{2\delta^2}\right) + T_0 \tag{3.13}$$

Due to the non-dimensionalization detailed Section 3.5, changes in voltage do not change the overall shape of density, velocity, and mass utilization quantities under study.

3.3 The steady state model

In order to provide the initial conditions for the time-dependent model where the oscillations occur, a steady state model with a converging solution must be established first. For the analysis done in this paper, the steady state model was comprised of ion and neutral continuity, ion momentum, and charge conservation equations. By way of Mathematica's **NDSolve** platform, this system of partial differential equations yielded interpolated functions for ion density, neutral density, ion velocity, and electron velocity. Several assumptions are required in this reduced form of the model.

"Initial" values for the plasma quantities in the steady state model refer to the assumed magnitude at the anode location of the channel, where $z = 0$.

The initial neutral velocity is assumed to be the thermal velocity of the neutral gas, delivered at room temperature, as described in Eqn. 3.14 . For both the steady state and

time dependent models, the neutral velocity is assumed to be constant through both the axial and temporal evolution of the channel. For ease of calculation, T_{room} is presented in Kelvin.

$$u_{n0} = \sqrt{\frac{k_B T_{room}}{m_i}} \tag{3.14}$$

Initial neutral density is calculated through Eqn. 3.15 from given outer (r_o) and inner (r_i) radii of the Hall thruster channel, assumed mass flow of the neutral gas $\dot{m}$, the ion mass m_i, and the initial neutral velocity. Due to the initial ions being delivered to the channel with the neutral gas, the initial ion velocity, u_{i0}, is assumed to be equal to the neutral velocity, u_{n0}.

$$n_{n0} = \frac{\dot{m}}{\pi(r_o^2 - r_i^2)m_i u_{n0}} \tag{3.15}$$

The initial electron velocity, u_{e0}, is the mean thermal velocity at the anode (Eqn. 3.16). The temperature is assumed to be at the minimum near the anode.

$$u_{e0} = \sqrt{\frac{2eT_{eV}}{\pi m_e}} \tag{3.16}$$

The initial plasma density is assumed from the discharge current at the anode (Eqn. 3.17), converted into a density through the initial electron velocity. Relating the initial plasma density to the current and the initial electron velocity yields initial plasma densities that match experimental results [6].

$$n_{i,steady} = n_{e,steady} = n_{steady} = \frac{I_d}{u_{e0}\pi(r_0^2 - r_i^2)} \tag{3.17}$$

3.4 The time-dependent model for oscillations

3.4.1 Boundary and Initial Conditions

The boundary conditions for the time-dependent models are defined to be identical to the boundary conditions of the steady state model used in that specific simulation. More details

on how those boundary conditions are crafted can be found in Section **??**.

The initial conditions for the time-dependent models are directly adapted from the steady state basis. For example, the initial distribution of the time-dependent plasma density function is identical to the steady state model. Thus, the time-dependent model can be seen as a time evolution of the steady-state system, given some additional perturbation.

3.4.2 Methods for Driving Oscillations

Driven oscillations can be induced in the time-dependent model through the following methods:

- Time-dependent oscillation in the location of the Gaussian peak of the electric field;
- Time-dependent oscillation in the boundary conditions for neutral or plasma density

Since the electric field function used a given location for the location of the Gaussian peak, z_a, replacing the location variable with a time-dependent function, such as $(\hat{z}_a \pm \hat{z}_s \sin \omega_s t)$, would cause the entire curve to oscillate periodically around the central point $\hat{z}_a$ at a frequency ω_s. Mathematically, the equation for the assumed electric field changes to Eqn. 3.18.

$$E_{var} = \frac{V_{dt}}{\sqrt{2\pi\delta^2}} \exp\left(-\frac{(z - (\hat{z}_a \pm z_s \sin \omega_s t))^2}{2\delta^2}\right) \tag{3.18}$$

The axial (linear) magnitude of the oscillation, $\hat{z}_s$, varies how far along axis the peak electric field moves, upstream and downstream, in the oscillation. The frequency of the oscillation, ω_s, governs how quickly the Gaussian curve moves along the axis. Variations in the axial magnitude and frequency and their effects on the time-dependent model are discussed in Sections 4.3 and 4.4, respectively.

Likewise, introducing an oscillation into the boundary conditions involves replacing the default conditions with a sinusoidal function based on time.

3.5 Non-dimensionalizing

Non-dimensionalizing of the system, which removes unit dependence from all of the fluid equations, is essential to extending the applicability of this model outside a particular geometry or neutral flow rate. In general terms, if x is a dimensional variable, the dimensionless equivalent, $\hat{x}$, is replaced through the following exchange:

$$\hat{x} = \frac{x}{x^*} \tag{3.19}$$

where x^* is the characteristic value for the system of the same dimensions as x. The characteristic values, such as characteristic length z^* and velocity u^*, are chosen for a specific system, and link this model to any other Hall thruster with known geometry and plasma characteristics.

A noteworthy added benefit of non-dimensionalizing the system comes from the various quantities staying within one or two orders of magnitude of 1. This prevents NDSolve from having to wrestle large numbers of wildly different magnitudes when trying to find an answer that converges, which reduces computational time and difficulty.

3.5.1 Characteristic Variables

The following characteristic variables are needed in order to satisfy the model:

Characteristic Electric Field, E_f^*, is the ideally linear electric field of the system, defined by the discharge voltage divided by the length of the channel. The units of the electric field are Vm^{-1} and is defined in Eqn. 3.20, where V_d is the discharge voltage (set in the model) and L, the total length of the channel.

$$E_z^* = \frac{V_d}{L} \tag{3.20}$$

Characteristic Density, n^*, is the ratio between the mass flow of the incoming neutrals, $\dot{m}$ (kg/s), and the product of the ion mass (kg), the channel cross-sectional area (m^2), and the initial neutral velocity(m/s), as defined in Eqn. 3.21. Using this characteristic density

(with units of m^{-3}) removes one of the largest magnitudes from the numerical solver, as densities are typically within an order of magnitude of 10^{17} m^{-3}.

$$n^* = \frac{\dot{m}}{m_i A u_n} \tag{3.21}$$

Characteristic Ionization Factor, R^*, is used to bring the very small magnitudes of the ionization rate (10^{-20}) to unity. The factor is assumed to be the ionization factor at peak electron temperature, T^*, and the units are $m^3 s^{-1}$, as defined in , Eqn. 3.22.

$$R^* = R_{ion}(T^*) \tag{3.22}$$

Characteristic Temperature, T^*, is the maximum temperature of the background electrons (with units of eV), which is also defined as a fraction of the discharge voltage, where c is greater than one (Eqn. 3.23).. General "rule of thumb" guidelines for Hall thruster design sets c 0.08 and 0.10; this model uses a $c = 0.08$.

$$T^* = cV_d \tag{3.23}$$

Characteristic Time, t^*, with units of seconds, is the characteristic time step of the simulation, defined to be a ratio of the characteristic velocity (Eqn. 3.25) and the characteristic length (Eqn. 3.26) as defined in Eqn. 3.24. Using a non-dimensionalized time allows simulations across a broad range of frequencies to still be qualitatively compared.

$$t^* = \frac{z^*}{u^*} \tag{3.24}$$

Characteristic Velocity, u^*, is the simplified thermal velocity of the ions in units of m/s (Eqn. 3.25), which is a product of the electron charge (q, C), voltage (V, volts), and the ion mass (m_i, kg). .

$$u^* = \sqrt{\frac{2qV_d}{m_i}} \tag{3.25}$$

Characteristic Length, z^*, is the length of the channel, L, from the anode (boundary condition) to the exit plane, in units of m. This is simply defined in Eqn. 3.26.

$$z^* = L \tag{3.26}$$

3.5.2 Non-dimensionalized Continuity Equation

The ion continuity (Eqn. 3.2) and neutral continuity (Eqn. 3.6) equations can be represented generically as:

$$\frac{\partial n}{\partial t} + \frac{\partial}{\partial z}(nu_z) = \pm n_i n_n R_{ion} \tag{3.27}$$

To non-dimensionalize this equation, Eqns. 3.21, 3.24, 3.26, and 3.22 are applied for each of the variables present: density, time, space, and the ionization factor, R, respectively. With the dimensionalized terms replaced, the equation transforms into Eqn. 3.28.

$$\frac{\partial \hat{n}}{\partial \hat{t}} + \frac{\partial}{\partial \hat{z}}(\hat{n}\hat{u}_z) = \pm(\frac{n^* R^*}{u^*/z^*})\hat{n}_i \hat{n}_n \hat{R}_{ion} \tag{3.28}$$

The factor that now appears on the right-hand side, $\frac{n^* R^*}{u^*/z^*}$, can be seen as a characteristic factor to describe the weight, or importance, of the ionization term for the system. The numerator of the factor, $n^* R^*$, can be seen as the ionization frequency of the system - how fast the neutral gas is ionizing. Likewise, the denominator, u^*/z^*, can be seen as the transit time across the channel length in the axial direction. Taken together, this implies that if the ionization frequency is too low, or the transit time is too fast for proper ionization to occur, then the ionization term in the continuity equations is very small, and vice versa.

3.5.3 Non-dimensionalized Ion Momentum Equation

The ion momentum equation, as stated in Eqn. 3.9, is:

$$\frac{\partial}{\partial t}(n_i u_{i,z}) + \frac{\partial}{\partial z}(n_i u_{i,z}^2) = \frac{e}{m_i} n_i E_z + n_i n_n R_{ion} u_n$$

Applying the non-dimensional relation for each of the variables in the form of Eqn. 3.19, the ion momentum equation transforms into Eqn. 3.29.

$$\frac{\partial}{\partial \hat{t}}(\hat{n}_i \hat{u}_{i,z}) + \frac{\partial}{\partial \hat{z}}(\hat{n}_i \hat{u}_{i,z}^2) = (\frac{E_z^*/u^*}{u^*/z^*})\frac{e}{m_i}\hat{n}_i \hat{E}_z + (\frac{n^* R^*}{u^*/z^*})\hat{n}_i \hat{n}_n \hat{R}_{ion} \hat{u}_n \tag{3.29}$$

The characteristic factor that evolves out of this momentum equation, $\frac{E_z^*/u^*}{u^*/z^*}\frac{e}{m_i}$, can be further simplified with a few assumptions. By applying the characteristic velocity equation, Eqn. 3.25, and the characteristic length, Eqn. 3.26, many terms cancel to leave only a ratio of the elemental charge and the discharge voltage, as shown in Eqn. 3.30.

$$\frac{E_z^*/u^*}{u^*/z^*}\frac{e}{m_i} = \frac{E_z^* z^*}{(u^*)^2}\frac{e}{m_i} = \frac{eVd}{2eVd} = \frac{1}{2} \tag{3.30}$$

3.5.4 Non-dimensionlized Charge Conservation

The non-dimensionalization of the charge conservation equation is best approached from the simplified equation, Eqn. 3.10:

$$\frac{\partial}{\partial z}(n_i u_i) = \frac{\partial}{\partial z}(n_e u_e)$$

Looking at the equation, since the terms of both derivatives are the same, any characteristic variables would be cancelled out. Therefore, the non-dimensionalized equation takes on the same form, but with the non-dimensionalized variables:

$$\frac{\partial}{\partial \hat{z}}(\hat{n}_i \hat{u}_i) = \frac{\partial}{\partial \hat{z}}(\hat{n}_e \hat{u}_e)$$

3.6 Computational Methods

Both the steady-state and time-dependent models used built-in Mathematica methods to numerically solve the set of PDEs described earlier in this chapter. The time-dependent model, in particular, could yield different results based on whether the method was explicit

or implicit solving the system, with greater variance than any of the other parameters (e.g. working precision, accuracy goals, or grid spacing).

For both the spatial and temporal grids, a minimum points of 200 was selected, as this produced smooth plots, comparable to 500 and 1000 grid points, but with the minimum amount of time.

3.7 Wall Loss Terms

There are several wall interaction terms that one can consider with this system, but this thesis is primarily focused on the energy loss due to collisions with the walls, P_{wall}. There are two possible approaches for this: Goebel [16] uses a geometry-averaged approach, where total quantities are already known (e.g. current into the wall for the entire thruster) along with average temperature in the channel. However, given the temporal and spatial detail available from the fluid model, a more precise approach can be used. Enter the approach influenced by Hara [20]: calculate the localized heat loss at each spatial point, S_{wall}, and then average these localized losses over the entire surface of the channel.

Hara [20] defines S_{wall} as:

$$S_{wall} = n_e \nu_{ew} \Delta\epsilon_w \tag{3.31}$$

Like many formulas in the plasma physics literature, this equation appears simple on its face but contains a few hidden assumptions. First, the electron density term in Eqn. 3.31 could appear to be the plasma density (it does, after all, appear in the electron total energy equation without qualifier), but using this number produces wall heat flux that is too high; the electrons in this quantity are, in fact, the electrons moving through the sheath at the channel walls. Second, the collisional frequency described here is calculated to be the velocity of the electrons towards the wall divided by the channel width, $U_{ew}/\Delta R$. As a frequency, the units of this term are s^{-1}, but if the $\Delta\epsilon_w$ term is in volts (as described in the paper), then the heat flux overall has units of $Jm^{-3}s^{-1}$, which contains one more length variable (m) than necessary for a heat flux ($Jm^{-2}s^{-1}$).

Therefore, to keep the units viable for a temporal and spatial integration when deriving power oscillations for this system (Section 3.7.1), a variation on Hara's equation, Eqn. 3.32, is used instead:

$$S_{wall} = en_{e,sh}U_{ew}\Delta\epsilon_w \tag{3.32}$$

where $n_{e,sh}$ is the electron density in the sheath, U_{ew} is the collisional velocity of the electron towards the wall, and $\Delta\epsilon_w$ is the mean electron energy loss due to electrons colliding with the wall. Finally, the entire equation must be multiplied by the electron charge in order to convert the units of volts (from $\Delta\epsilon_w$) to joules. This form is also functionally identical to Goebel's approach when integrated over the entire length of the channel.

The electron-wall collisional velocity can be found through calculations involving the ion species velocities. Starting with the ion velocity at the sheath edge, U_{iw}, the Bohm velocity is assumed to be the species velocity, defined as:

$$U_{iw} = \sqrt{\frac{eT_{eV}}{m_i}} \tag{3.33}$$

where T_{ev} is the temperature of the plasma and m_i is the mass of the ion species [20]. This ion velocity can then be modified with the secondary electron emission coefficient, σ, to yield the electron mean velocity toward the wall at the sheath edge, U_{ew}. This is also defined in Hara [20] as:

$$U_{ew} = \frac{U_{iw}}{1-\sigma} \tag{3.34}$$

$$U_{ew} = \frac{\sqrt{\frac{eT_{eV}}{m_i}}}{1-\sigma} \tag{3.35}$$

The secondary electron emission coefficient, σ, is defined in this particular model according to Hara's specifications for xenon, Eqn. 3.36 [20]. This coefficient, also referred to as the secondary electron "yield," describes how many electrons are released from a material per

incident (oncoming) electron. This generosity (or lack thereof) from the material dictates the potential of the sheath along the channel walls, which in turn affects the electron flux and heat flux towards the wall. Furthermore, the material's reaction is neither constant nor linear: σ at temperatures higher than $20eV$ is steady. This implies that a large portion of the acceleration region, where electric field and temperature peak, experiences the same secondary electron emission. [16]

$$\sigma = Minimum(0.54 + 0.46\frac{T_{eV}}{20}, 0.986) \tag{3.36}$$

In the equation given by Goebel [16], the sheath potential is a function of temperature, and since the temperature in this model is a function of location, so, too, is the sheath potential (Eqn. 3.37). Already, dramatic differences in localized wall flux loom, which could lead to hotter areas of the channel wearing down earlier from added thermal stress.

$$\phi_s = -T_{eV} \ln [\sqrt{\frac{2m_i}{\pi m_e}} \frac{n_e}{n_e + n_s} \frac{\nu_B}{\nu_i}(1 - \sigma)] \tag{3.37}$$

In Eqn. 3.37, n_e is the density of the electrons in the sheath, n_s is the density of secondary electrons coming from the channel wall through the sheath, ν_B is beam, or axially-oriented, ion velocity, and nu_i is the ion velocity at the sheath edge. For the case of using xenon in a dielectric-lined SPT, Goebel provides the simplifying assumption of Eqn. 3.38, where the momentum of the electrons going into the sheath from the beam is roughly half of the momentum of the primary and secondary electrons leaving the sheath.

$$\frac{n_e}{n_e + n_s} \frac{\nu_B}{\nu_i} = \frac{1}{2} \tag{3.38}$$

Taking this assumption, then simplifying the square root, leads to the sheath potential equation used by Hara [20] and the code at the focus of this thesis (Eqn. 3.39).

$$\phi_s = -T_{eV} \ln[\frac{(1 - \sigma)}{\sqrt{2\pi \frac{m_e}{m_i}}}] \tag{3.39}$$

Once the sheath has been calculated, the electron density in the sheath can be found. The electrons in the sheath are some factor of the plasma density in the beam, affected by both temperature and sheath potential (Eqn. 3.40) [16].

$$n_{e,sh} = n_p \exp\left(\frac{\phi_s}{T_{eV}}\right) \tag{3.40}$$

It is of the utmost importance that the density used in the calculation of this wall term is *not* the plasma density; rather, the density of the ions penetrating through the sheath towards the wall must be used. Using the unadulterated plasma density inflates the resulting flux and power calculations, resulting in nonsensical power values that are (for instance) greater than the input power (derived from the discharge voltage and current). This electron density can then be used in the calculation of the wall flux described in Eqn. 3.32.

Once the sheath potential is known, the electron energy loss to the wall can also be calculated [20]:

$$\Delta\epsilon_w = 2T_{ev} + \phi_s \tag{3.41}$$

or, expanded with Eqn. 3.39:

$$\Delta\epsilon_w = T_{ev}[2 + \ln\left(\frac{1-\sigma}{\sqrt{2\pi\frac{m_e}{m_i}}}\right)] \tag{3.42}$$

From examining Eqn. 3.42, energy loss appears to vary proportionately with σ, in contrast to the inverse proportionality of the electron-wall collision frequency. The equation also shows that in the ideal case where you have no secondary electron emission ($\sigma = 0$), energy loss due to wall collision would still occur.

3.7.1 Power Assessment

The overall power being lost to the walls at any one point in time can be calculated from the heat flux into the walls integrated over the length of the channel, L, multiplied by the

circumference of both the inner and outer walls of the annular channel, as described in Eqn. 3.43 .

$$P_{wall}|_t = 2\pi(r_o + r_i) \int_0^L S_{wall}|_t \, dz \tag{3.43}$$

To analyze how this power fluctuates with time, the integration is completed separately for each individual time step. The range of the time steps, ideally, would be from $\hat{t} = 0$ to $\hat{t} = \hat{t}_{max}$ at the prescribed number of grid points; this may not be possible for some evaluations where the initial time steps in the time dependent solution show very high gradients before the solution converges. At the very least, it would give a false sense of the range of power values over the temporal range of the system.

Within this model, given the lack of constraints on channel potential that would bring results closer in line with experimental results, the power loss oscillations will be compared to the steady state power losses. This allows for more self-consistent conclusions about the impact of oscillations on the plasma.

Chapter 4

DRIVEN OSCILLATIONS IN THE 1D FLUID MODEL

4.1 Steady State Model Baseline

With the fixed, Gaussian electric field static in the channel, the fluid model roughly aligns with experimental research on the quantities defined below [6] [37]. Graphs of the quantities contain the location and width of the defined acceleration region: the center is represented by the dashed line and the boundaries around it are $\hat{\delta}$ distance from the center.

Plasma density (Fig. 4.7) increases linearly from the initial set value, reaches a peak before the acceleration region (at a distance of approximately one-tenth of the full channel length), then drops dramatically due to the growing electric field and, therefore, the growing acceleration on the ions and electrons. Once crossed over the acceleration region, there is a brief negative deviation in the value before the plasma density falls to a steady value. This steady density is maintained from the end of the acceleration region to the exit plane of the thruster.

The expontential increase of the plasma density can be attributed to the linear definition for the ionization term given by the model. The increase continues unhampered due to the narrow width of the electric field's non-negligible magnitude. (elaborate more on local maximum since it factors in the wall loss terms)

The neutral density plot (Fig. 4.8)for the steady state is even simpler, remaining relatively flat and unchanging until the plasma reaches the acceleration. At the boundary of the region, the neutral density begins to fall, likely from the sudden increase in collisions between neutrals and electrons. This increase in collisional frequency would create more ions, which are then spirited away quickly by the intense electric field in this area.

Like the plasma density, once the plasma steps out of acceleration region, neutral density

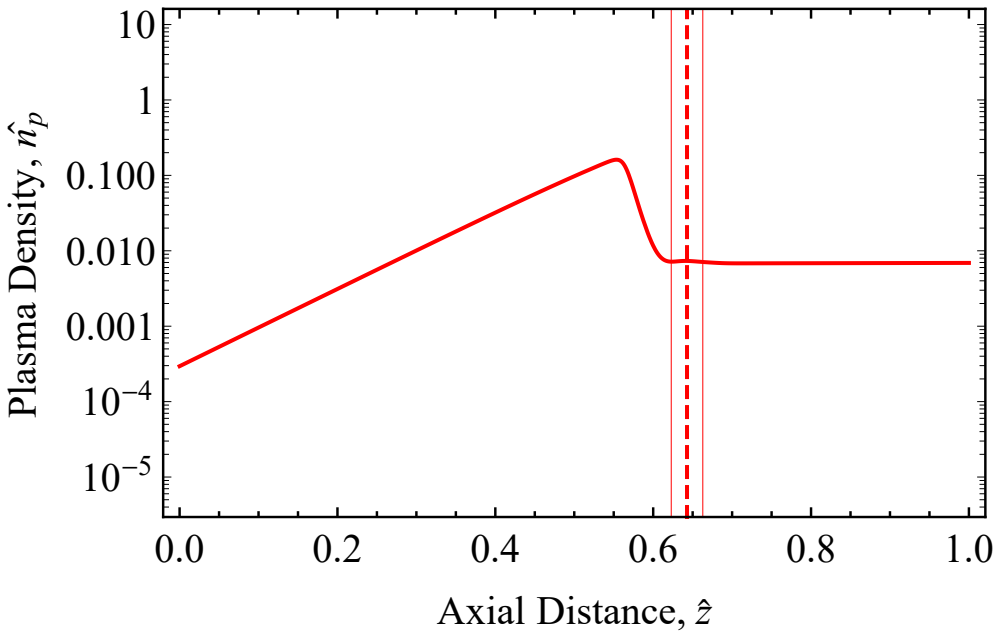

Figure 4.1: Steady state model results for plasma density, non-dimensionalized.

remains steady and unchanging through the exit plane of the thruster. The flat nature of the neutral density, both before and after the acceleration region, is unsurprising given the neutral species' indifference to potential difference.

By contrast, the ion velocity does respond acutely to the electric field and changes therein. Outside of the acceleration region, where the electric field magnitude is negligible, the ion velocity remains virtually flat, first with the initial velocity of the neutral species, then its exit plane velocity at approximately 85% of the Bohm velocity. The transition between these two velocities occurs in the short width of the acceleration region, increasing quasi-exponentially from the same axial position as where the plasma density drops post-maximum. Experimentally, the ions continue to accelerate albeit at a much slower pace, and this is likely not captured because the boundaries of the simulation only include the thruster channel itself [9].

The electron velocity is best examined "backwards," that is, working from $\hat{z} = 1$ towards the start of the thruster channel $\hat{z} = 0$. Between the exit plane and the border of the

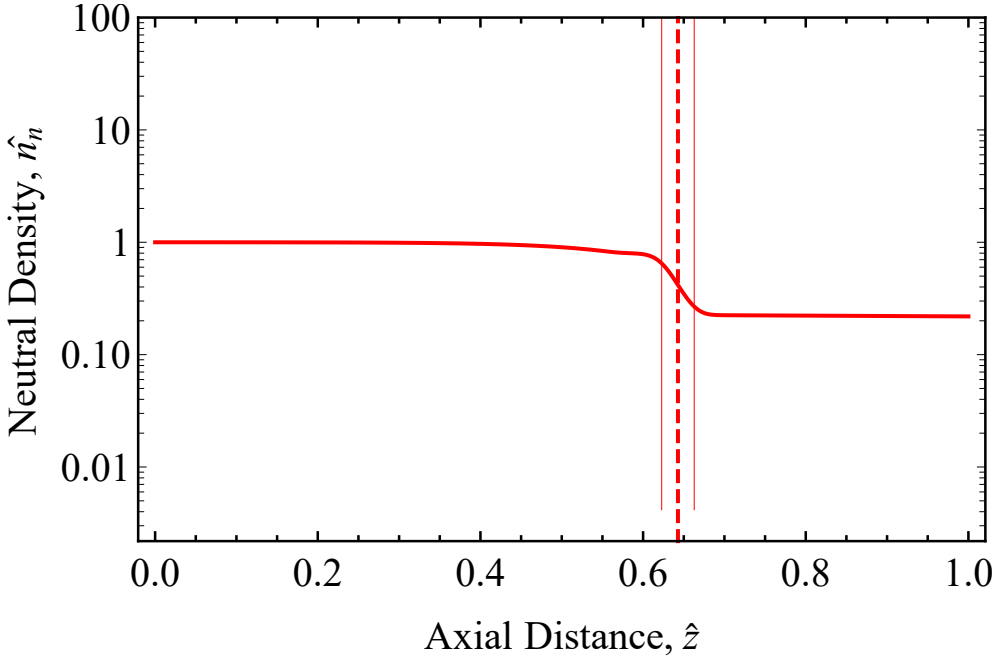

Figure 4.2: Steady state model results for neutral density density, non-dimensionalized.

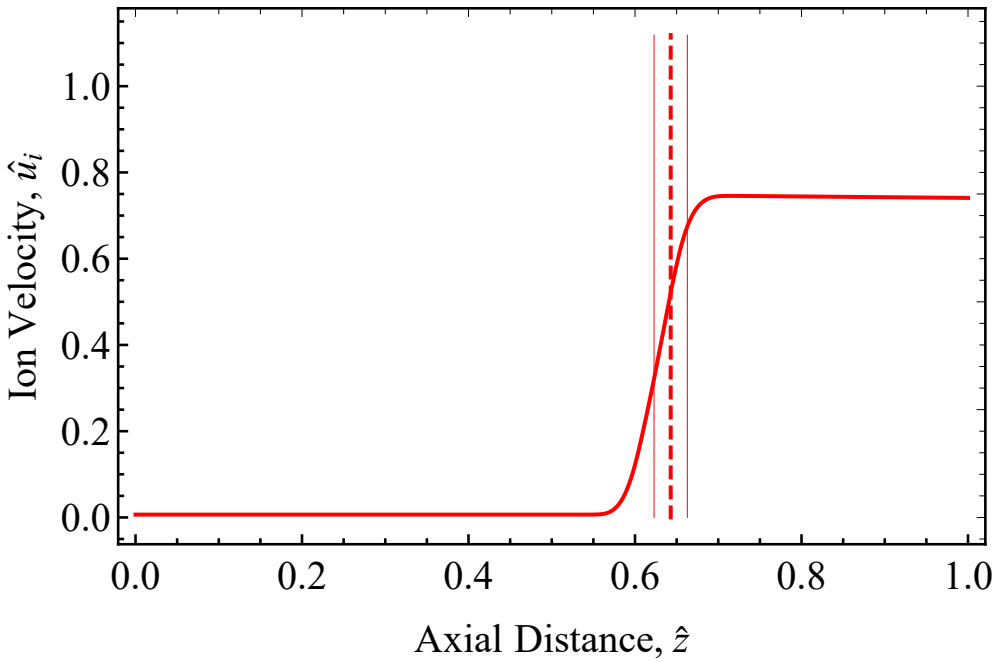

Figure 4.3: Steady state model results for ion velocity, non-dimensionalized.

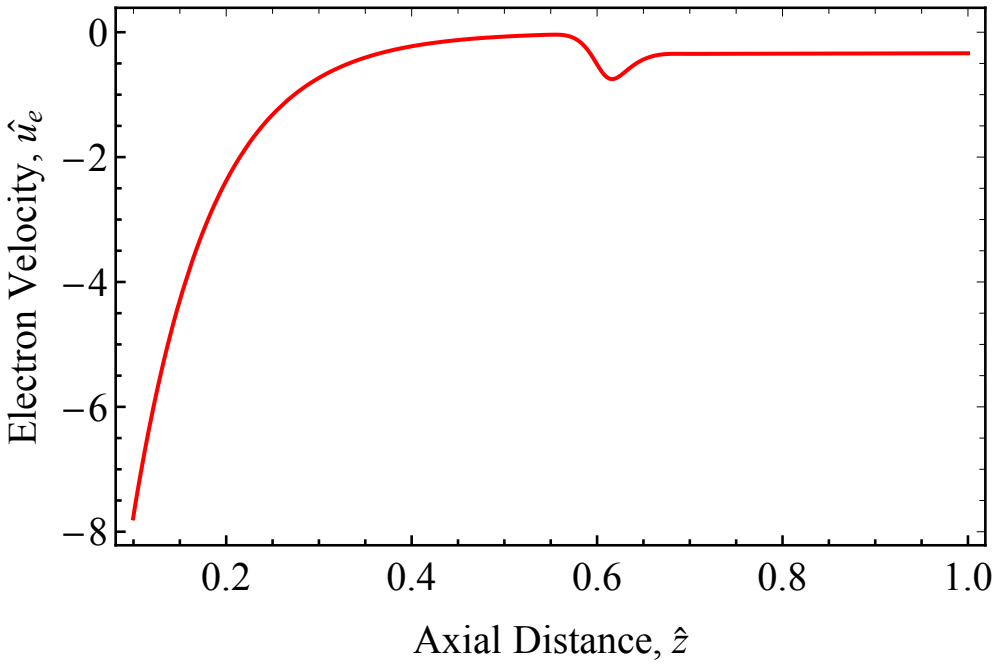

Figure 4.4: Steady state model results for electron velocity, non-dimensionalized.

acceleration region, the electron velocity is steady; this is not prescribed anywhere in the model, but is likely due to the same effects that maintain a steady ion velocity and plasma density in the same region: the electric field magnitude is negligible, and the potential is virtually static.

Within the acceleration region, electron velocity exhibits a slight decrease in overall magnitude (an increase in vector notation, since the velocity vector is pointing towards the anode). Just outside the region, velocity magnitude grows to an equivalent magnitude of the Bohm velocity, then exponentially decays to less than 10% of the Bohm velocity at approximately the same location as the ion density increase.

Unlike the ion velocity, the region between the anode and the acceleration region do not exhibit steady values for the electron velocity. While the potential change here is as negligible as near the exit plane, the distance between the electrons and the anode, r, is decreasing. Since the electric force scales with r^2 and it acts on the extremely light electron mass, the

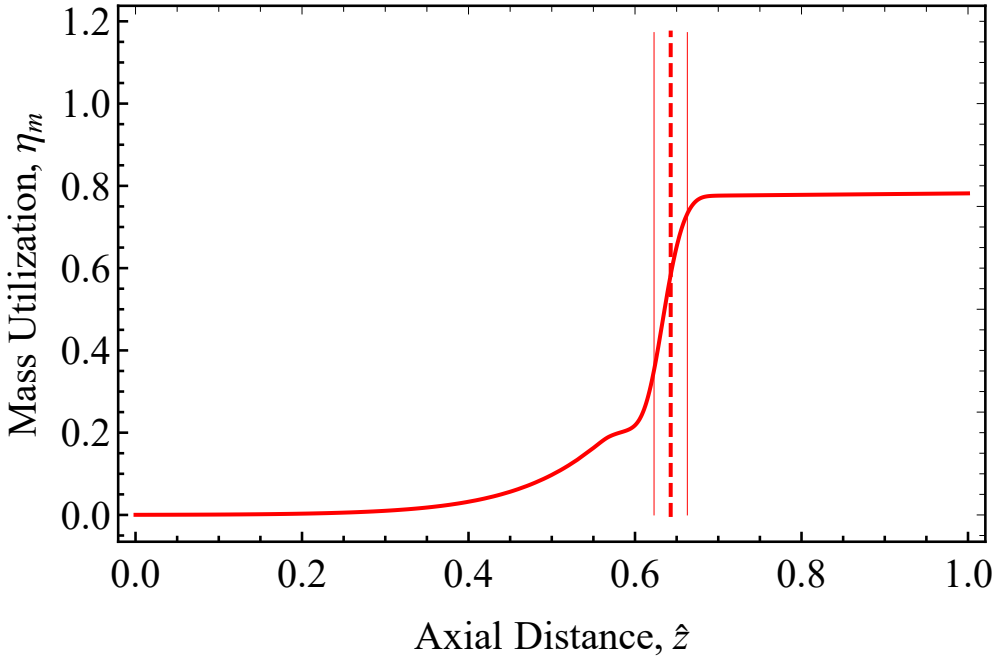

Figure 4.5: Steady state model results for mass utilization, non-dimensionalized.

electron velocity increases exponentially towards the anode ($\hat{z} = 0$). At the boundary, the electron velocity reaches over nine times the Bohm velocity (as prescribed by the numerical solver).

The mass utilization for the system follows the general shape of the ion velocity, though it increases earlier in the channel length before increasing steeply in the acceleration region. After the acceleration region, mass utilization flattens to a steady value of approximately 0.8. Compared to the experimental results for the SPT, which hover around 50% [29], this seems quite favorable. However, knowing wall losses will cut into this efficiency makes 0.8 less than ideal. Changing the thruster length has shown to affect the exit plane mass utilization, but those efforts are not the focus of this thesis.

4.2 Steady State Model: Boundary Condition Variations

4.2.1 Initial Plasma Density

The following charts are created with thruster quantity set according to Section 3.2.1. Within the steady state model, the initial ionization boundary condition, n_0, which determines the initial charged species density at the anode of the thruster, was varied from a default condition of approximately 0.0003 of the initial neutral density.

Analytical observation of the ion continuity equation (Eqn. 3.2) shows that there must be *some* non-zero amount of charged species density in order for the model to converge; this is borne out in the simulation results as well – in a null solution set. However, n_0 cannot be too high, either, as this produces unrealistic results: an initial density of 0.1 leads to mass utilization values above 1.0, which violates the conservation of energy for the system. The near breakdown of $n_0 = 0.1$ and the total breakdown of $n_0 = 0.5$ with regards to mass utilization can be seen in Fig. 4.6.

Limiting the range of the boundary condition to $\pm 50\%$ of the default value, a modest variation in the quantities appear. The plasma density starts out split according to the boundary condition, but post-acceleration region levels to nearly the same value for all variations (Fig. 4.7). Neutral density (Fig. 4.8) and ion velocity (Fig. 4.9) shows a reverse trend with the divergence in magnitudes appearing post-acceleration. Electron velocity (Fig. 4.11) shows the greatest spread, but again only in the post-acceleration region, whereas the three conditions merge into a singular velocity as the electrons approach the anode.

4.3 Time Dependent Model: Axial Displacement Dependency

Axial displacement cases in this section were simulated according to the thruster geometry established in Section 3.2.1, with a time range of 5 cycles. The default linear translation displacement, $\hat{z}_s$, is 0.001 m, and the nominal frequency is set to $10,000 Hz$. The minimum displacement case has the axial displacement set to 0.0005 m, while the maximum displacement case is set to 0.005 m. This maximum was chosen for this section's analysis because it

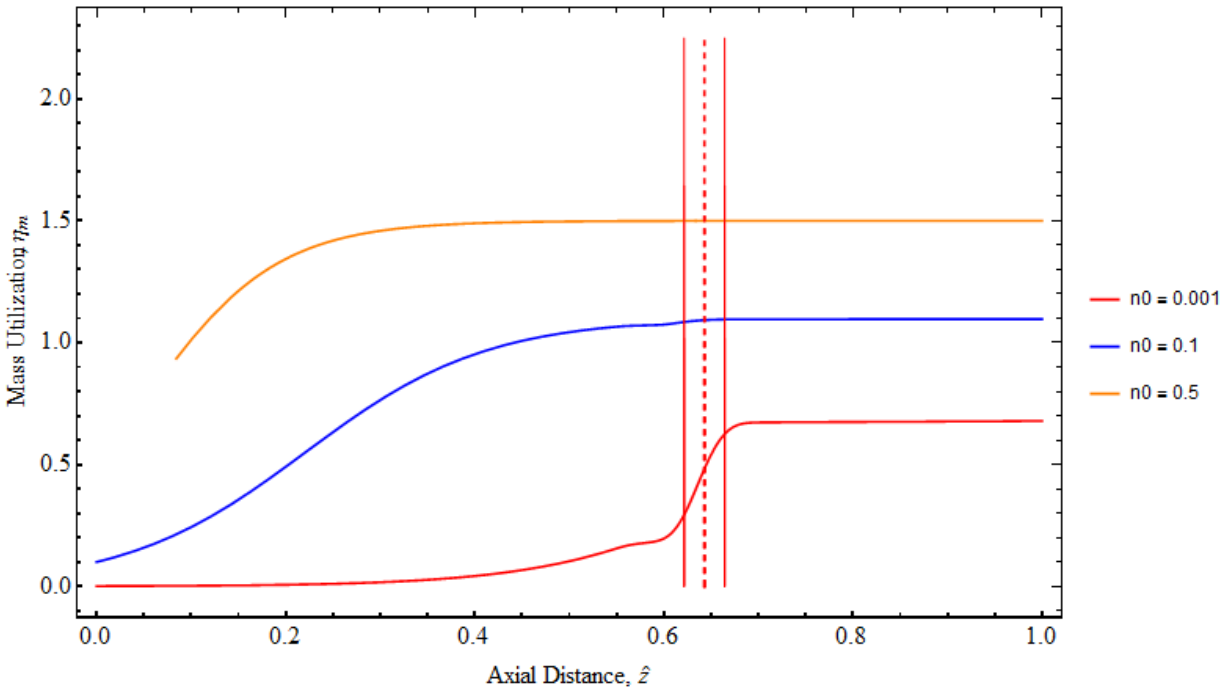

Figure 4.6: The breakdown of the model, as seen through the mass utilization quantity. For the steady state model, mass utilization above 1.0 is physically impossible, suggesting that the system has a maximum initial plasma density.

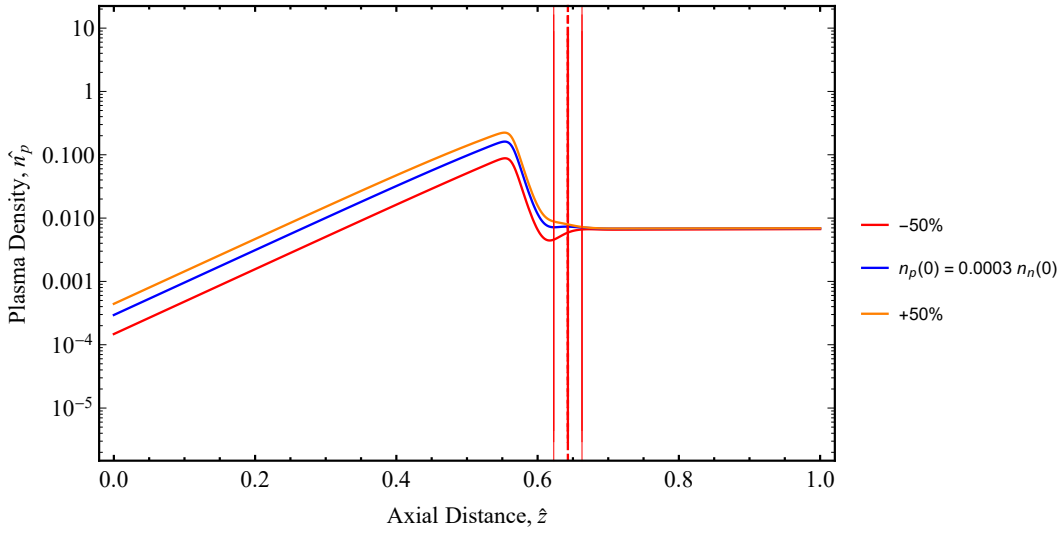

Figure 4.7: The steady state model for plasma density with a varying initial plasma density.

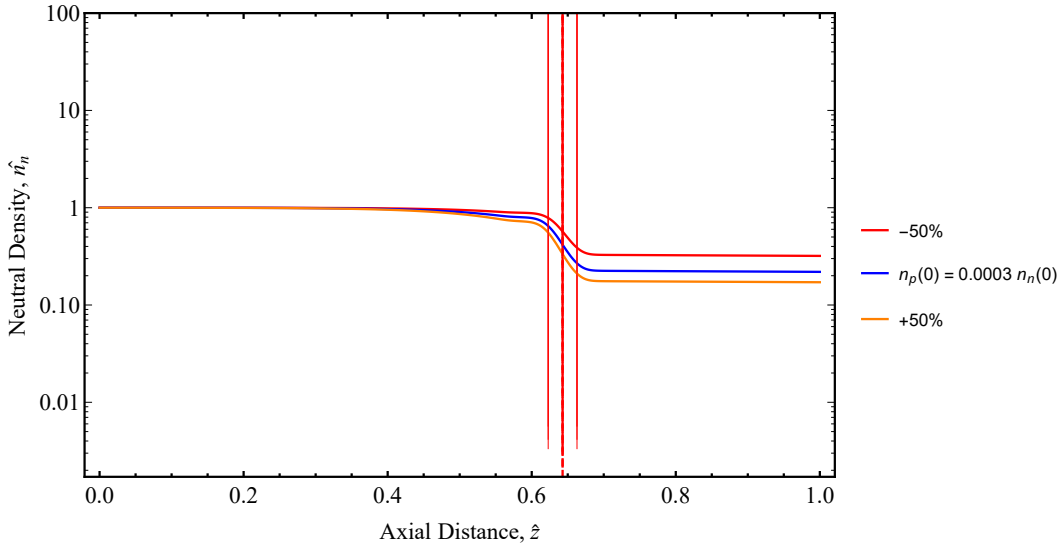

Figure 4.8: The steady state model for neutral density with a varying initial plasma density.

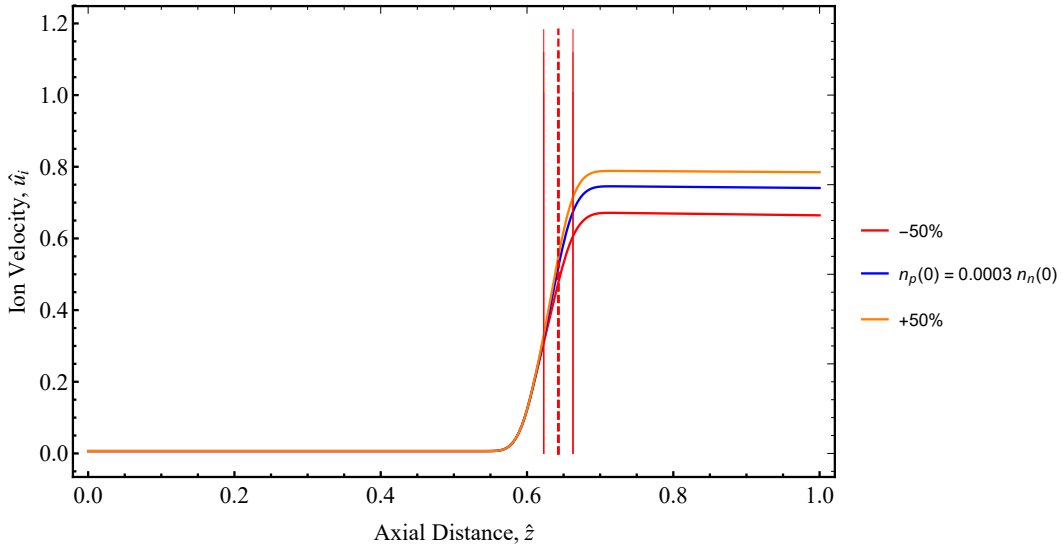

Figure 4.9: The steady state model for ion velocity with a varying initial plasma density.

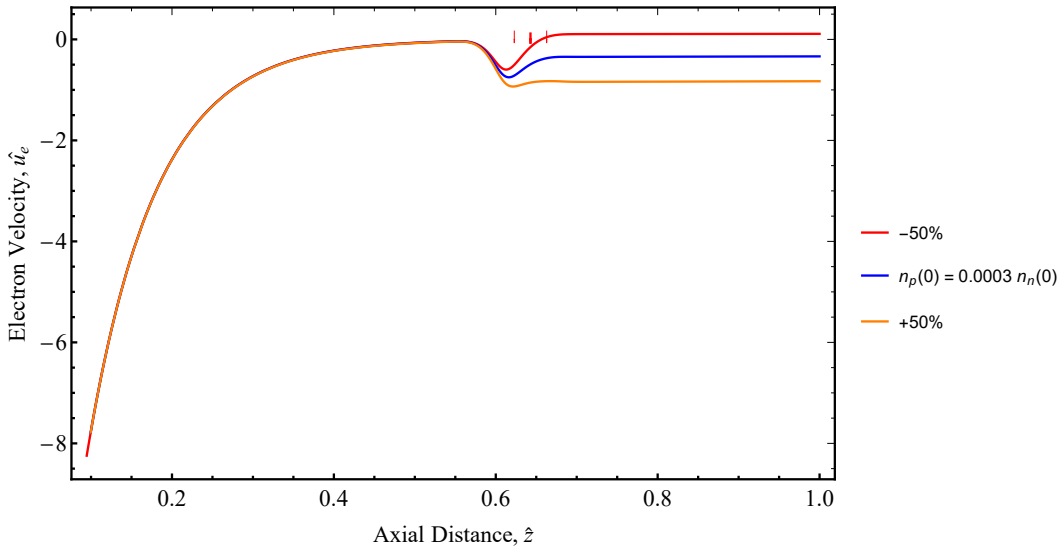

Figure 4.10: The steady state model for electron velocity with a varying initial plasma density.

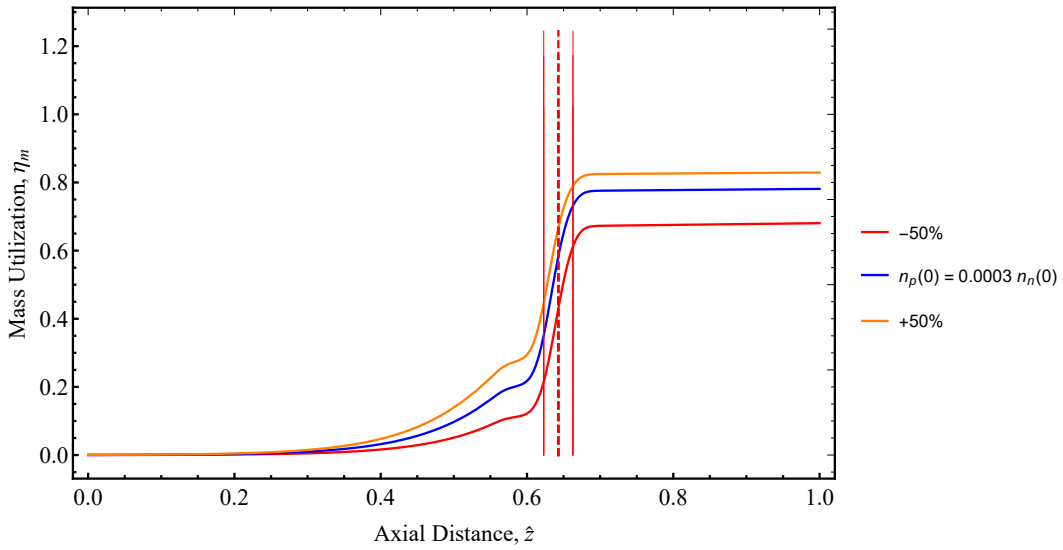

Figure 4.11: The steady state model for mass utilization with a varying initial plasma density.

showcases extreme distortion in the pseudo-sinusoidal signal within the physical bounds of the system.

The graphs in this section are taken both at the location of the peak electric field (from the steady case) and at the thruster exit plane. The blue dashed line across the graph represents the steady state value at the same location.

4.3.1 Axial Displacement Variation: Neutral Density

The neutral density within the acceleration zone (Fig. 4.12) appears sinusoidal for the minimum and nominal displacement cases, oscillating roughly symmetrically about the steady-state mean value. In contrast, the maximum displacement case shows a highly asymmetric oscillation, with the amount of time spent below the mean steady value decreasing as the neutral density moves from the center of the acceleration region (Fig. 4.12) to the thruster exit plane (Fig. 4.13).

Both locations also show an interesting feature as the density decreases from the peak magnitude: a brief (less than 10 μs) leveling of the slope before the steep decrease towards the trough continues. This minor stall in the neutral density implies that the ionization process itself maybe be dramatically slowing down or stalling. This rate change could be caused by a spike in plasma density; as seen in the corresponding plasma density graphs (Figs. 4.14 and 4.15), these irregularities appear to align with the peaks of the plasma density signal.

At the exit plane in particular, the neutral density signal does not establish an oscillating signal until roughly 150 μs into the simulation. This apparent lag, along with the trough value that is lower than the oscillating signal trough, could originate simply because it takes time for perturbations in the density to travel down the length of the channel. What, then, leads to extreme density trough at the upstream location? Looking at the first cycle (0 to 100 μs), the driven oscillation pushes the electric field Gaussian towards the exit plane, which also pushes up the characteristic ramp up of the plasma density (seen in the steady state model, Fig. 4.8, due to an increased temperature and ionization rate) further towards the exit plane as well; this allows the local neutral density to increase. In the second half of that

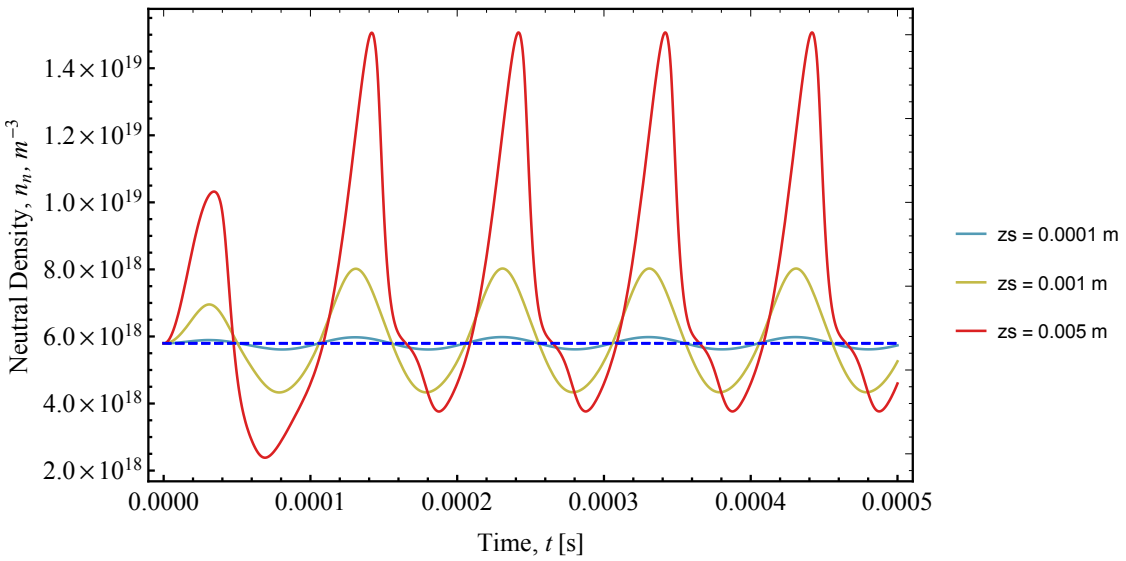

Figure 4.12: Neutral density at the peak electric field location with varying linear translation distance.

cycle, however, that region of intense ionization swings back through the nominal location (leading to the trough minimum) and further still: now that the high temperature ionization region sits upstream of the location being monitored, the density starts to increase towards the steady state equilibrium again.

Finally, the signal at both locations appears to "lean" forward, that is, approaching the peak at a more gradual slope than when its decreasing from the peak. This, again, may be due to the nature of the oscillation and the fact its moving a Gaussian distribution along the axis, introducing non-linear effects in the change of the neutral density.

4.3.2 Axial Displacement Variation: Plasma Density

At both the peak electric field location (Fig. 4.14) and at the exit plane (Fig. 4.15), the plasma density exhibits very sharp peaks and broad troughs for the maximum displacement case, while the nominal and minimum displacement cases are sinusoidal about the steady mean value. In comparison to the maximum displacement case, the minimum displacement

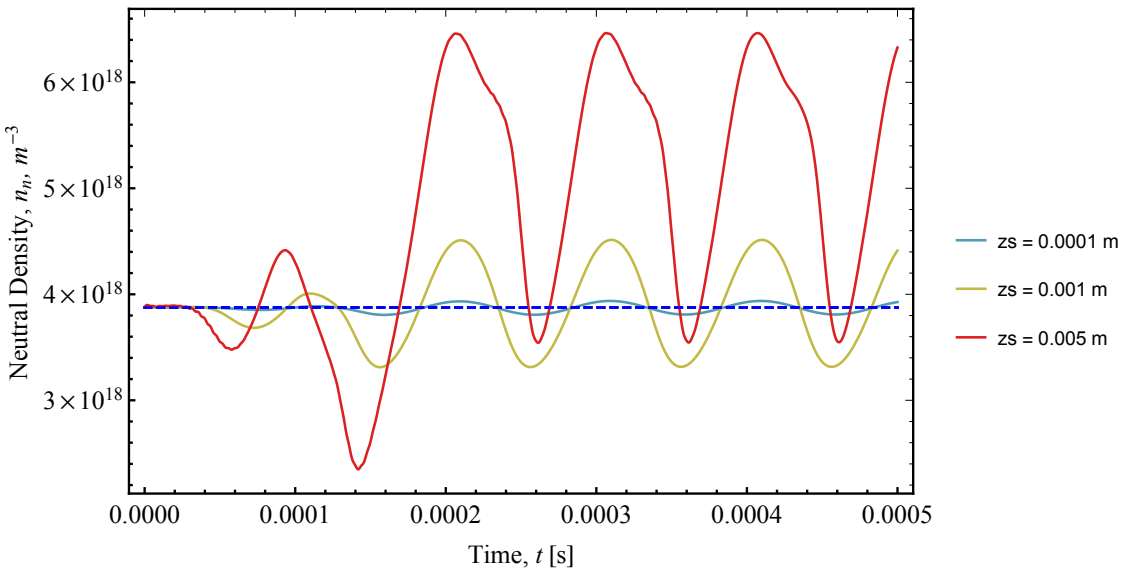

Figure 4.13: Neutral density at the thruster exit plane with varying linear translation distance.

case barely moves in magnitude from the mean value.

Notably in the maximum case, the start-up behaviors differ: at the upstream location the plasma density peak starts at a higher value than the equilibrium peak, while at the exit plane the starting peak is at a lower magnitude than the equilibrium peak. Like the neutral density oscillations, this could be due to the first driven oscillation pushing the peak electric field towards the exit plane, allowing the build-up of ions seen in the steady state model (Fig. 4.7) to extend further along the channel, which are then swiftly accelerated out of the thruster once the electric field Gaussian moves upstream. Since the following oscillations are building up from the trough values and *not* the mean equilibrium value, the peaks do not reach the same magnitude as the initial peak. Likewise, at the exit plane, the initial plasma density is both closer to the equilibrium value and does not benefit from upstream perturbations, so the initial peak is at a lower magnitude than subsequent peaks.

The presence and shape of the peak itself implies that the larger the displacement becomes, the more of a "whiplash" effect the plasma density experiences. As the peak electric

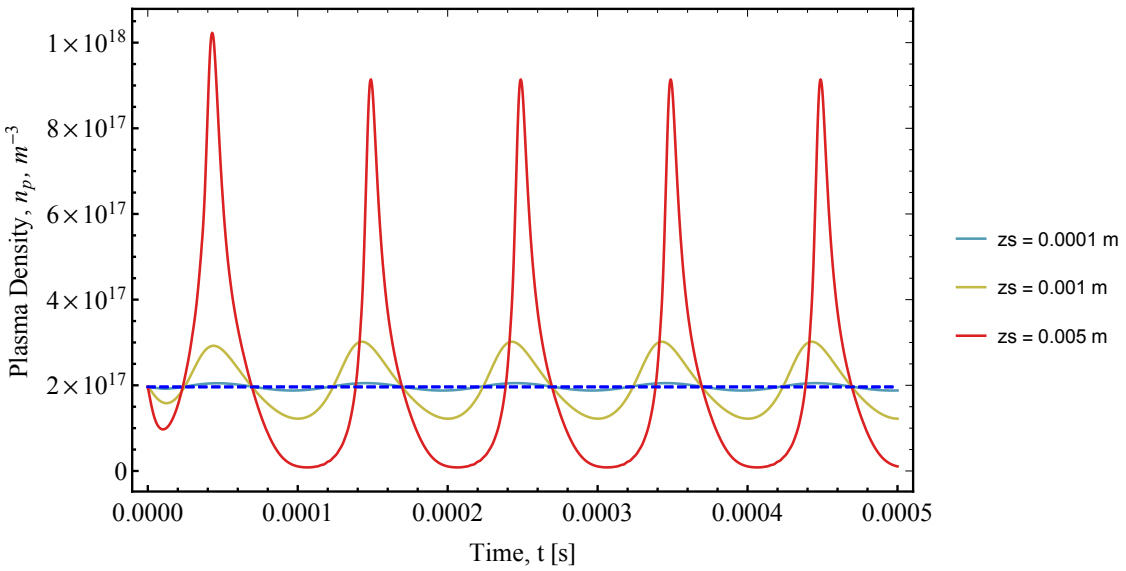

Figure 4.14: Plasma density at the peak electric field location with varying linear translation distance.

field moves downstream towards the exit plane, plasma density builds upstream. Then, when the electric field moves upstream again, those additional ions are accelerated out of the thruster. The broad stretch of the trough, then, implies that the now-elongated region of low potential dampens any growth in plasma density until the electric field can swing back towards the exit plane. This whiplash likely produces the irregularities of the neutral density and ion velocity signals, as discussed in their respective sections.

4.3.3 Axial Displacement Variation: Ion Velocity

The greatest qualitative discrepancies between the displacement cases appear in the ion velocity graphs. The minimum displacement case barely moves from the mean equilibrium value at either the peak electric field location (Fig. 4.16) or the exit plane (Fig. 4.17), but this constancy does not carry into the other cases. With the nominal displacement case, the signal starts off as very sinusoidal but deviates at the exit plane, spreading out the peak into a pseudo-plateau. Finally, the maximum displacement case introduces not only familiar

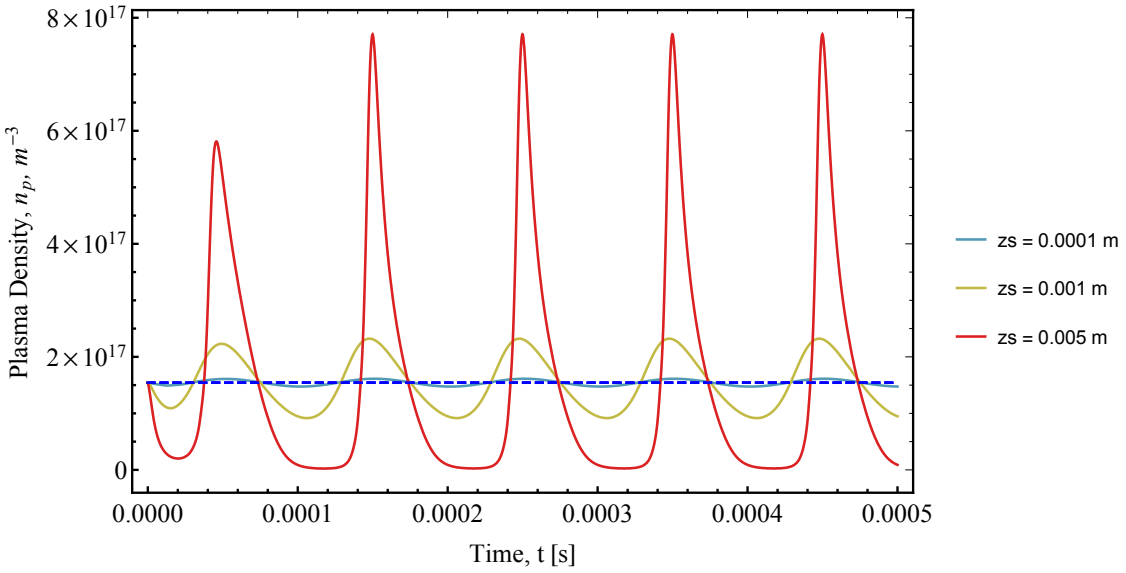

Figure 4.15: Plasma density at the thruster exit plane with varying linear translation distance

irregularities that have been discussed previously, but local maximum as the signal increases from its (comparatively, very slow) trough magnitude.

At the z_a location, the oscillations in the ion velocity align (in temporal evolution) approximately with the driven oscillations: when the electric field Gaussian moves towards the exit plane, the ion velocity drops, and when it moves further upstream, the velocity rises. Furthermore, within the first oscillation the signal shows the "stall" when it decreases from the peak magnitude, much like the neutral density and ion velocity graphs at the exit plane, further suggesting that the appearance of this irregularity in those graphs originates further upstream.

Unlike the z_a location, the exit plane ion velocity exhibits unstable start-up oscillations in the same fashion as the neutral density at the exit plane (Fig. 4.13), and for a similar amount of time (100 μs). What is more peculiar, however, is the appearance of two oscillation cycles within that span of time when the driven oscillation has only gone through one cycle. The first miniature cycle stretches between 0 to 50 μs, which is roughly the time it takes for the electric field Gaussian to travel from the nominal value, to the exit plane, and return. This

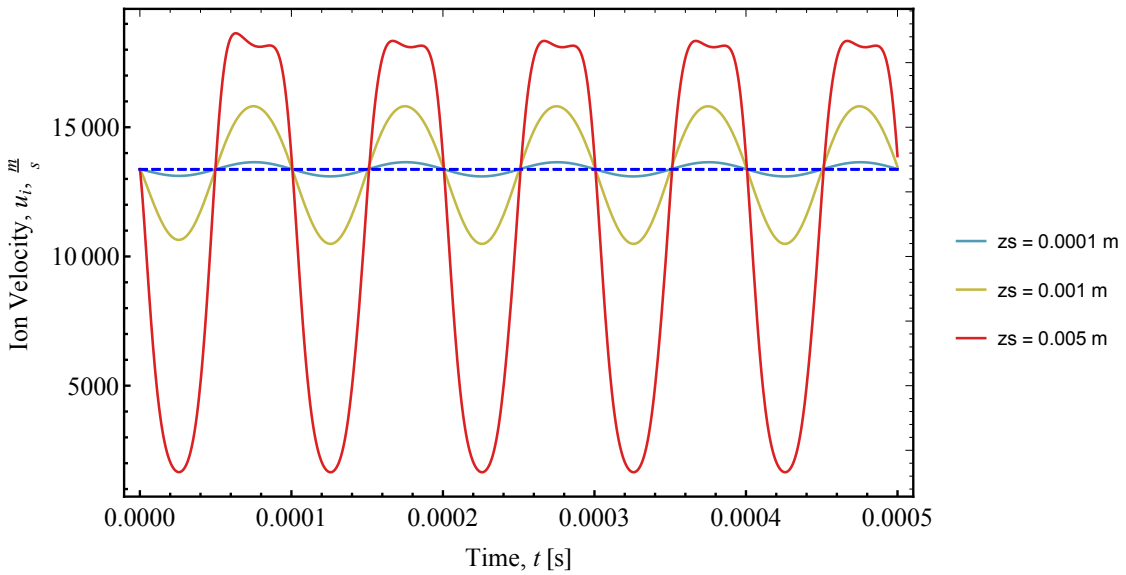

Figure 4.16: Ion velocity at the peak electric field location with varying linear translation distance.

implies that the proximity, and not merely the overlap, of the peak electric field can greatly accelerate ions in the same manner as seen in the steady state model (Fig. 4.9). The next miniature oscillation, from 50 to 100 μs, corresponds with the peak electric field moving from the nominal location, upstream, and back. With this oscillation, the probable causes for its oscillation are more directly tied to the upstream plasma velocities, which lead to an initial increase at 50 μs, but then also lead to deeper trough as the electric field moves further and further away in the cycle.

When the oscillating signal finally stabilizes, a new irregularity appears as the signal rises from the trough to mean value, first seen between 160 and 180 μs. Possible causes are unclear, though one explanation could be that this is an effect of the quasineutrality imposed by Eqn. 3.10: the magnitude of the electron velocity at around this same time (see Fig. 4.19) oscillates around zero, forcing the ion velocity to also oscillate briefly to correctly match the electrons.

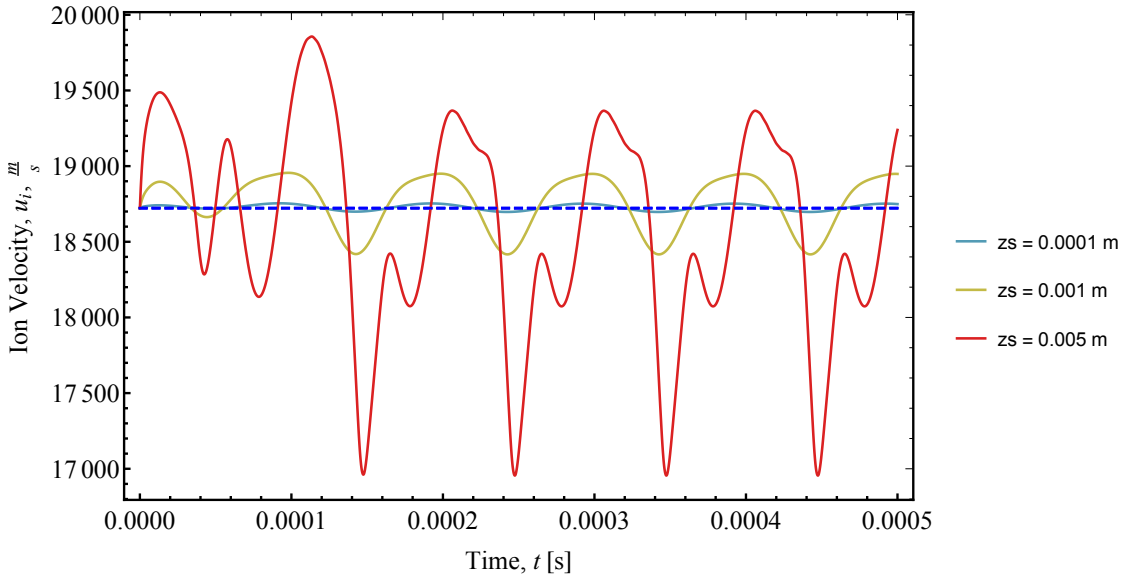

Figure 4.17: Ion velocity at the thruster exit plane with varying linear translation distance.

4.3.4 Axial Displacement Variation: Electron Velocity

The electron velocity graphs shows the most extreme range for magnitudes out of all of the graphs, both in the case-to-case variation and the location-to-location variation. Due to the highly negative magnitudes reached by the maximum displacement case, the magnitudes for the nominal and minimum displacement cases nearly disappear into the steady state equilibrium value (the blue dashed line). Furthermore, the maximum displacement case shows an increase in velocity of an order of magnitude (from 10^5 to 10^6 m/s) as the location shifts from upstream (Fig. 4.19) to the exit plane (Fig. 4.19).

As mentioned in the section regarding the ion velocity, the extremes in the maximum displacement case may originate from a non-linear combination of factors, including the sharp peaks of the plasma density and the very low troughs of the ion velocity. In order to balance this in the charge conservation equation (Eqn. 3.10), the electron velocity must swing dramatically.

In addition, the electron velocity is highly sensitive to the strength of the electric field,

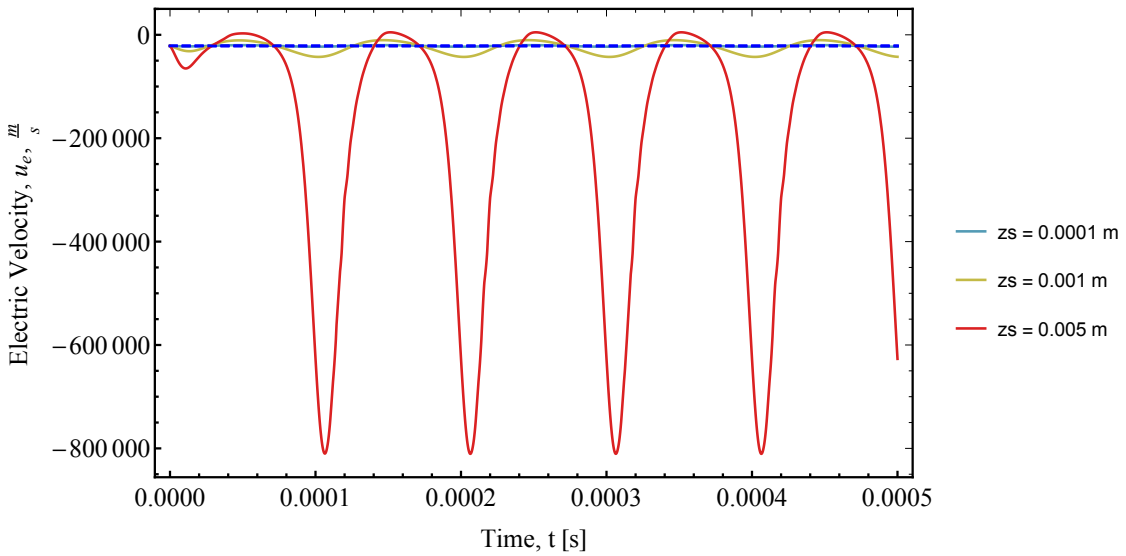

Figure 4.18: Electron velocity at the peak electric field location with varying linear translation distance.

due to the electron's small mass. Therefore, the greatest (most negative) electron velocities of each graph appear to align with the occurrence of the the peak electric field coming the closest to the location being watched.

4.3.5 Axial Displacement Variation: Mass Utilization

At both $\hat{z}$ locations of the peak electric field and the exit plane of the thruster, mass utilization follows a similar trend as the other quantities: as the plasma density peaks and falls, so does the mass utilization, with very shapes (i.e. the broad trough) (Fig. 4.20).

Note that in this time dependent scenario the mass utilization can momentarily peak above 1 to as high as 4 - that is, the momentum in that instant is multiples greater than the momentum of the incoming neutral gas to the thruster. While the average of this signal still remains at the steady state value, the spikes in the mass utilization further illustrate a "breathing" mode, where instead of expelling ions at a constant rate, the thruster releases ions in waves.

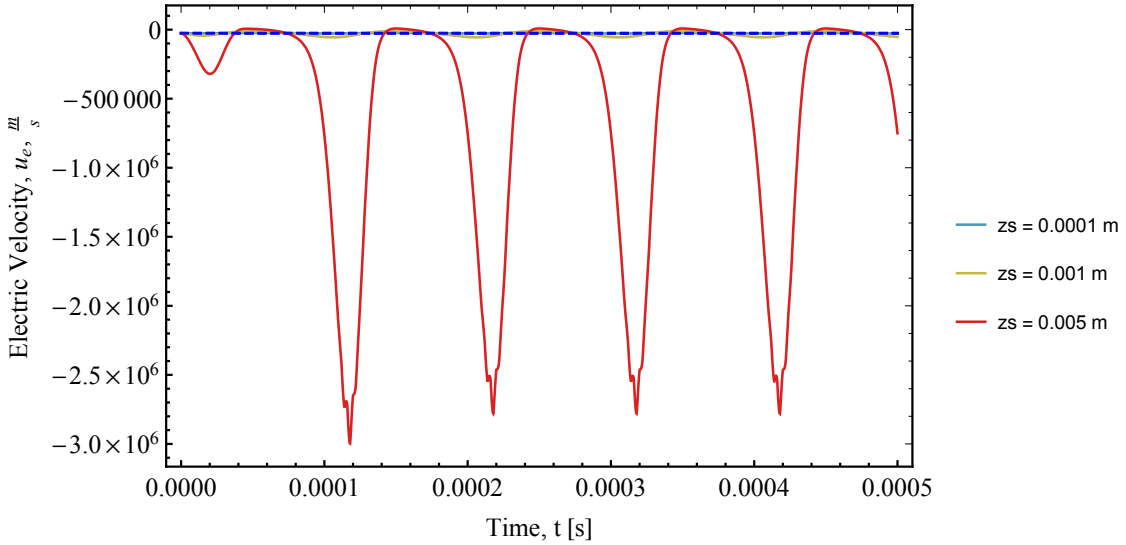

Figure 4.19: Electron velocity at the thruster exit plane with varying linear translation distance.

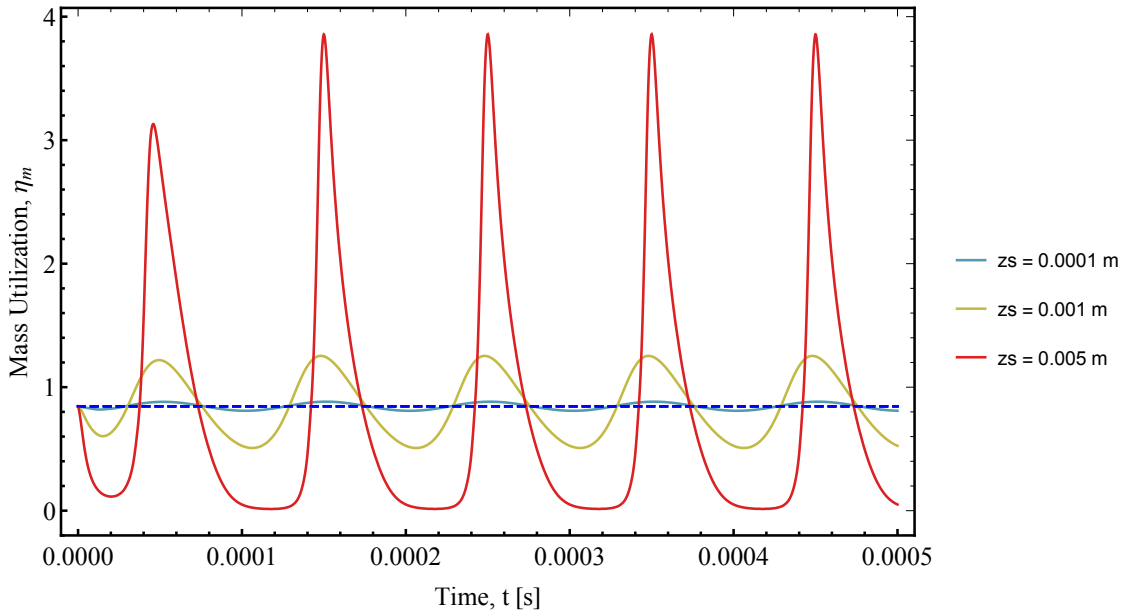

Figure 4.20: Time-dependent mass utilization with varying linear translation distance.

4.4 Time Dependent Model: Frequency Dependency

For these simulations, the axial displacement was set to the nominal distance (0.001 m) while the frequency was varied from 1 kHz to 50 kHz, the broadest range of the breathing mode as described in the literature [6].

Compared to the axial displacement case, little changes in the qualitative shape of the quantities as the frequency increases, with the obvious exception that the peaks and troughs occur more frequently with increased frequency. By magnitude, the effects are mixed. The peak magnitudes of the plasma density and the electron velocity grow with increasing frequency, while the neutral density and the ion velocity fall with the same conditions. Mass utilization also grows since plasma density rises more than ion velocity falls. Looking at the extreme case of 50 kHz, these results could be due to the fact that, as the frequency increases, the system starts to see a pseudo-steady state broadening of the electric field Gaussian function, which raises the mean temperature of the plasma within $\pm z_s$ distance of the peak. This, too, broadens the area with the fastest ionization rate, which leads to an increase in plasma density and a corresponding decrease in neutral density.

One would expect that the ion velocity would also increase, since this strong electric field is a primary factor in the acceleration, but the results do not support this idea: ion velocity actually drops with increased frequency. Perhaps, rather than the width of the Gaussian, the peak magnitude of the electric field is more indicative of ion velocity; the smeared, pseudo-steady Gaussian of the high-frequency case would yield an average peak magnitude that isless than the steady state. The influence of these changing magnitudes on the power loss is discussed in Chapter 5.

In the neutral density graphs at the exit plane (Fig. 4.22), the lag appearing in the neutral density for the 50 kHz case is very visible but also misleading: the 50 kHz case has such a short cycle time that the lag is expected, since it does take a finite time for the perturbation to travel along the thruster channel (approximately 200 m/s for the 50,000 kHz case).

Unlike the huge perturbations shown in the axial displacement, the plasma density does not show any significant differences between either the upstream or exit plane locations. The only notable feature is the sharp trough of the 10 kHz signal at the thruster exit location (Fig. 4.24).

In a similar trend, the ion velocity signals for the frequency cases is much more stable and sinusoidal than the axial displacement case. Almost all of the cases are very sinusoidal with the exception of the 50 kHz signal at the exit plane (Fig. 4.26): there is another start-up irregularity, similar to the start-up cycles for the extreme axial displacement case (Fig. 4.17). It also hints at the "stalling" slope shown in the axial displacement cases, which offsets the peak-side of the oscillation.

The electron velocity also does not show the extreme swings in magnitud that are exhibited in the axial displacement. Across all the frequency cases (Fig. 4.28) the electron velocity remains within the same order of magnitude of the steady state value. The largest range appears in the 50 kHz signal at the exit plane, which oscillates across a range of 30 kHz around the steady state value.

Due to the stability of the ion velocity and the plasma density across the cases, the mass utilization also exhibits a stable oscillation with few notable irregularities. Similar to the maximum axial displacement case, the 50 kHz case exhibits instantaneous mass utilization values above 1.

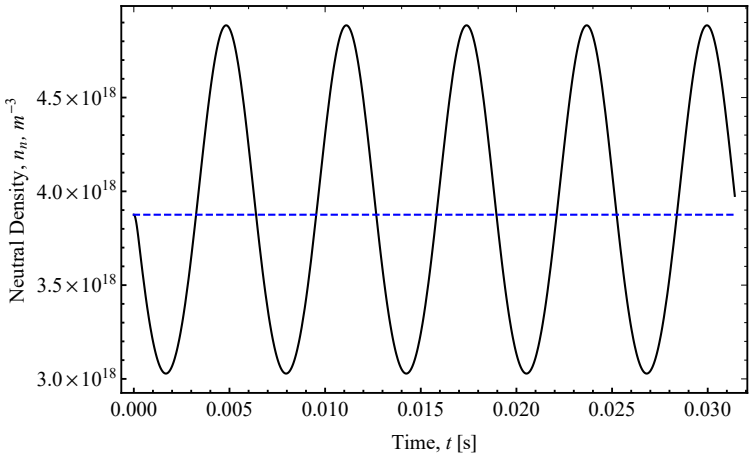

(a) 1 kHz

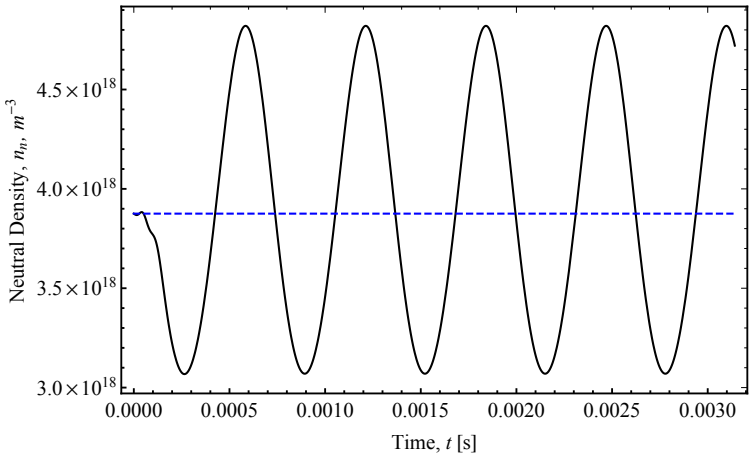

(b) 10 kHz

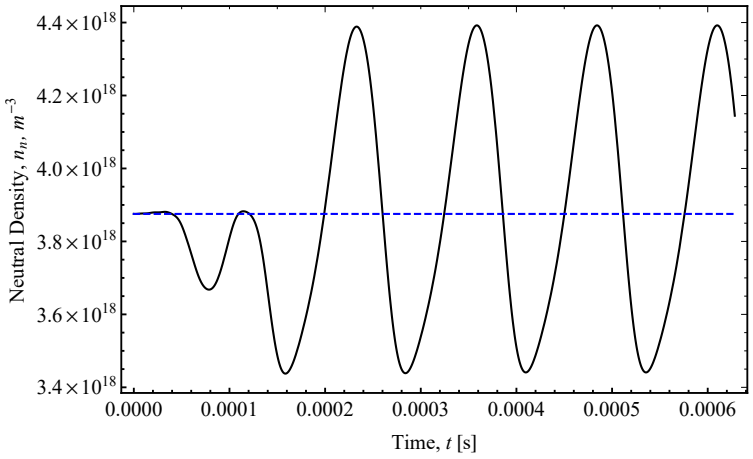

(c) 50 kHz

Figure 4.22: Neutral density at the thruster exit plane at (a) 1 kHz, (b) 10 kHz, and (c) 50 kHz.

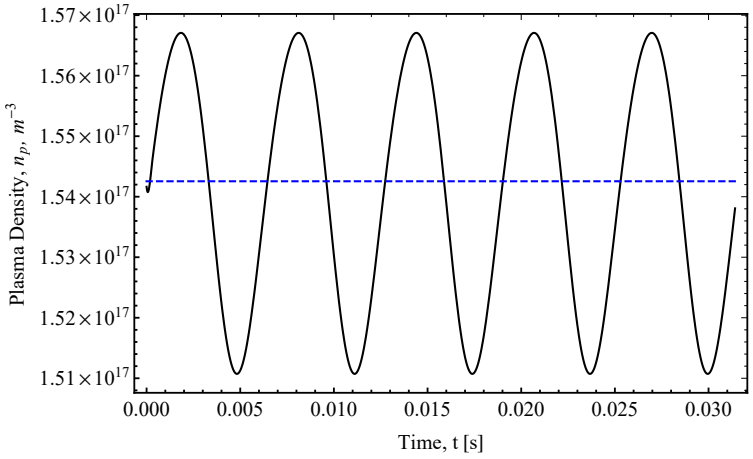

(a) 1 kHz

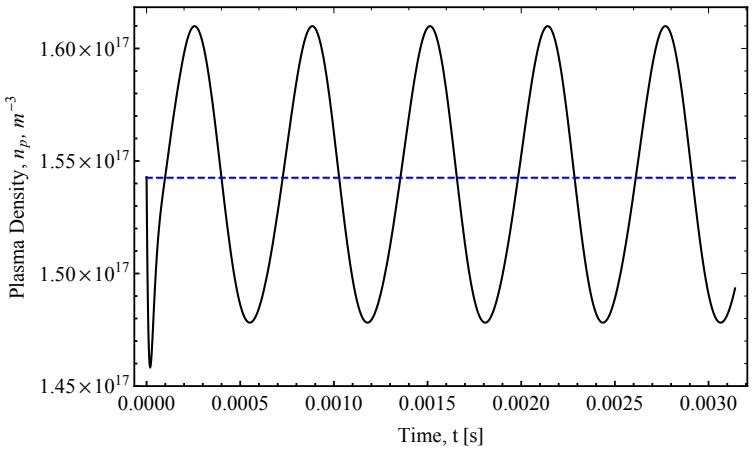

(b) 10 kHz

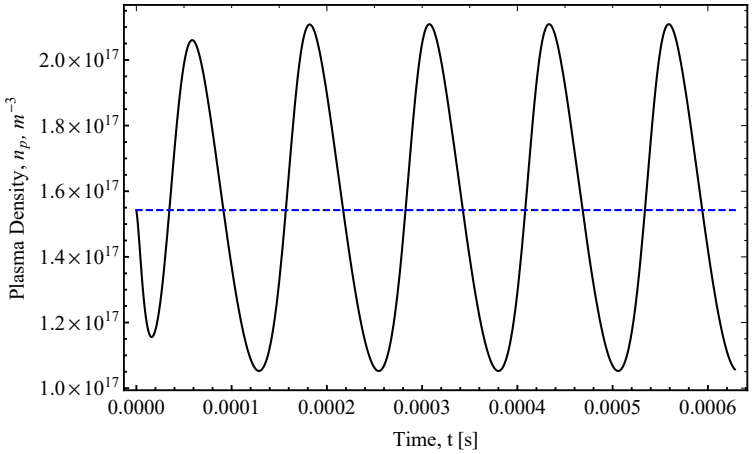

(c) 50 kHz

Figure 4.24: Plasma density at the thruster exit plane at (a) 1 kHz, (b) 10 kHz, and (c) 50 kHz.

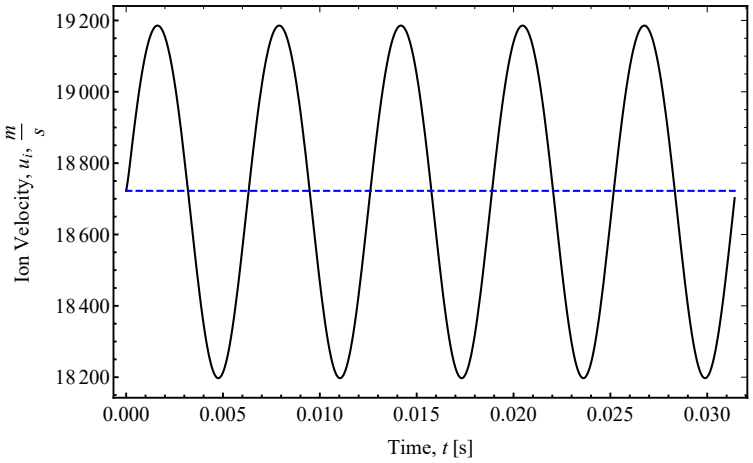

(a) 1 kHz

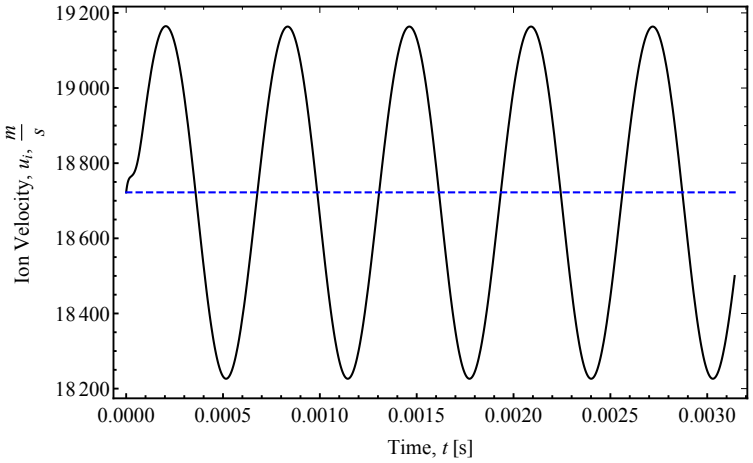

(b) 10 kHz

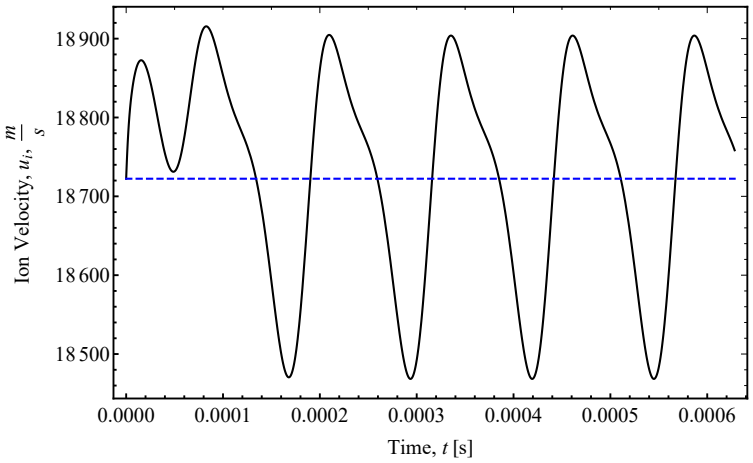

(c) 50 kHz

Figure 4.26: Ion velocity at the thruster exit plane at (a) 1 kHz, (b) 10 kHz, and (c) 50 kHz.

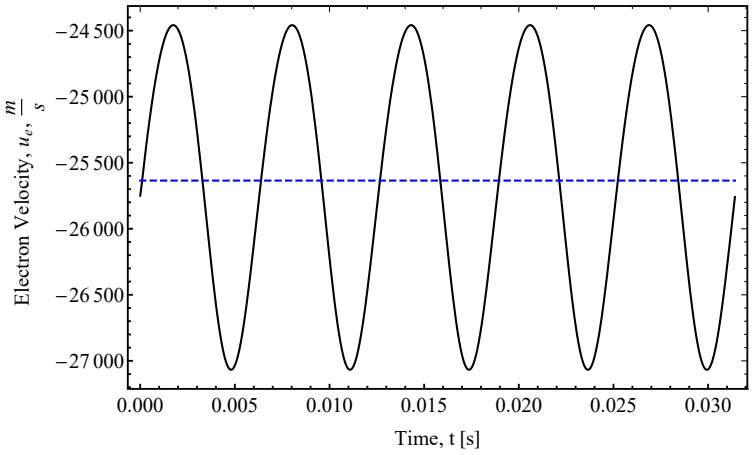

(a) 1 kHz

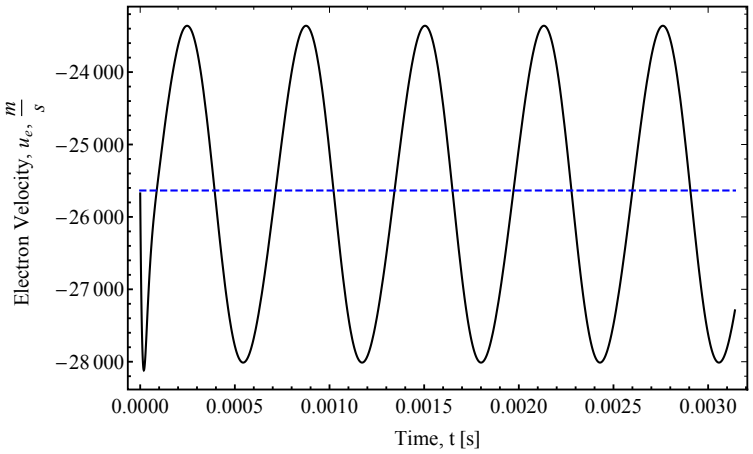

(b) 10 kHz

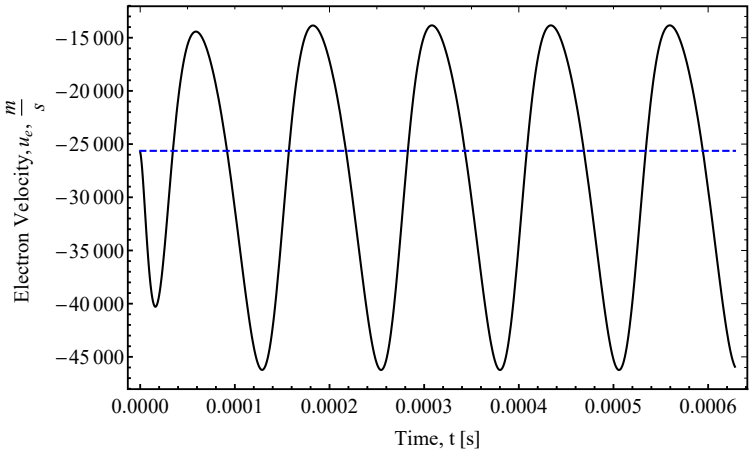

(c) 50 kHz

Figure 4.28: Electron velocity at the nominal peak electric field location (z_a) at (a) 1 kHz, (b) 10 kHz, and (c) 50 kHz.

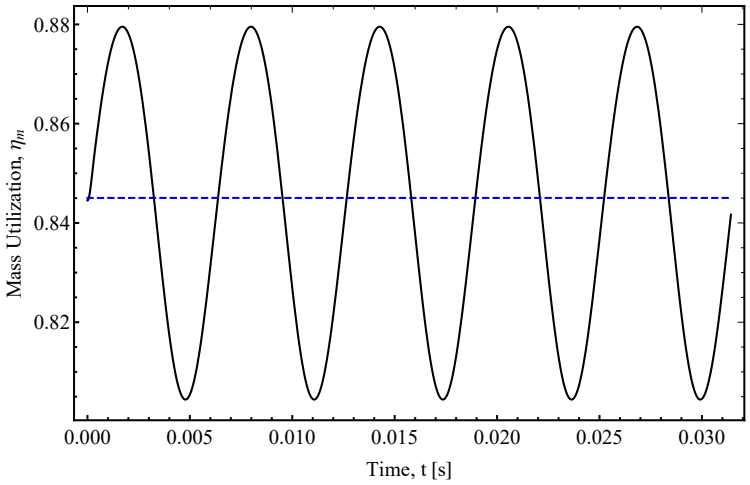

(a) 1 kHz

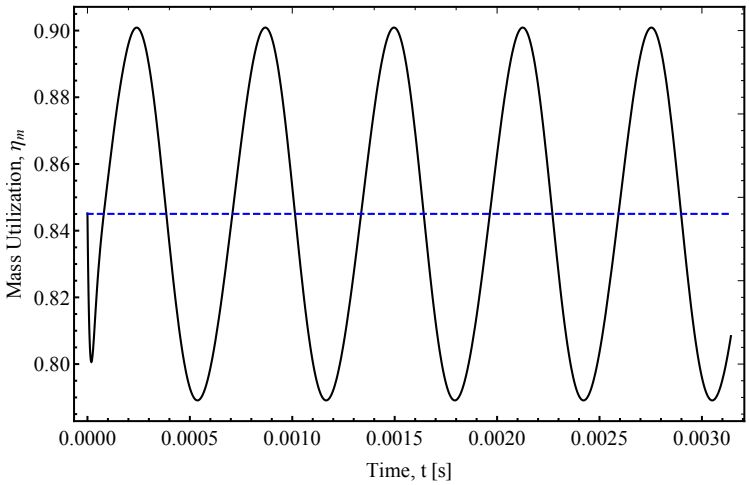

(b) 10 kHz

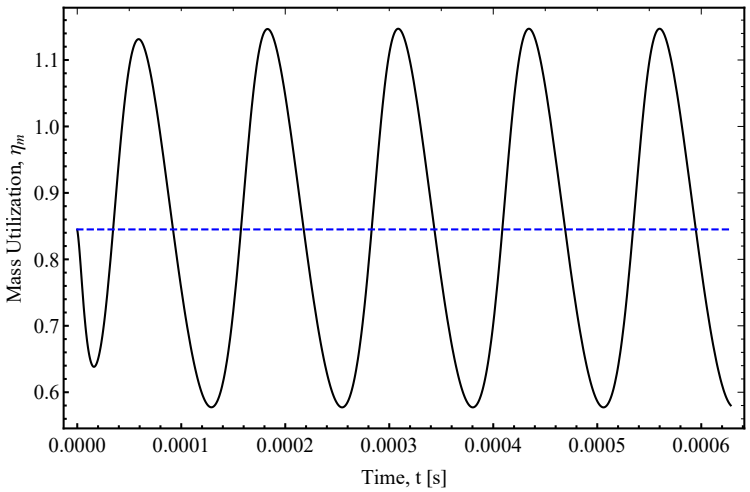

(c) 50 kHz

Figure 4.30: Mass utilization at (a) 1 kHz, (b) 10 kHz, and (c) 50 kHz.

Chapter 5

BREATHING MODE EFFECTS ON THE WALL LOSS TERMS

As stated in Section 3.7, power loss to the channel walls is calculated from multiple factors, each derived from non-linear functions and plasma quantities that have been shown to change under perturbation. Therefore, to better understand the effects that frequency variation and axial displacement have on power loss, each term in the calculation should be considered separately. How do these terms change on a local level, and what consequences does that have for the overall system over space and time? How sensitive is the power loss mechanism to these perturbations?

5.1 Effects on Electron-Wall Collisional Frequency

Examining the dependencies for Eqn. 3.34, temperature affects the collisional frequency through the ion and electron velocities, both contributing factors. Temperature directly increases the ion velocity at the wall by a half power, which in turn also increases the electron velocity (directly related to ion velocity through Eqn. 3.34). Notably, the secondary electron emission also conveys yet more influence from temperature until reaching a maximum value of σ_{max}, the maximum secondary electron emission coefficient, 0.986 in this model.

Therefore, the collisional frequency should trend with temperature along the thruster axis. This can be seen in Fig. 5.1, which also shows the abrupt change in the function shape once $T_{eV} = 20eV$. This is the limit for the minimum function defining σ (per Eqn. 3.36), when the steady value is used rather than the temperature-dependent function. However, since the other contributing factor to the collisional frequency, ion velocity towards the wall (the Bohm velocity), is still dependent on temperature, the function continues to rise, albeit as $T_{eV}^{1/2}$ instead of T_{eV}.

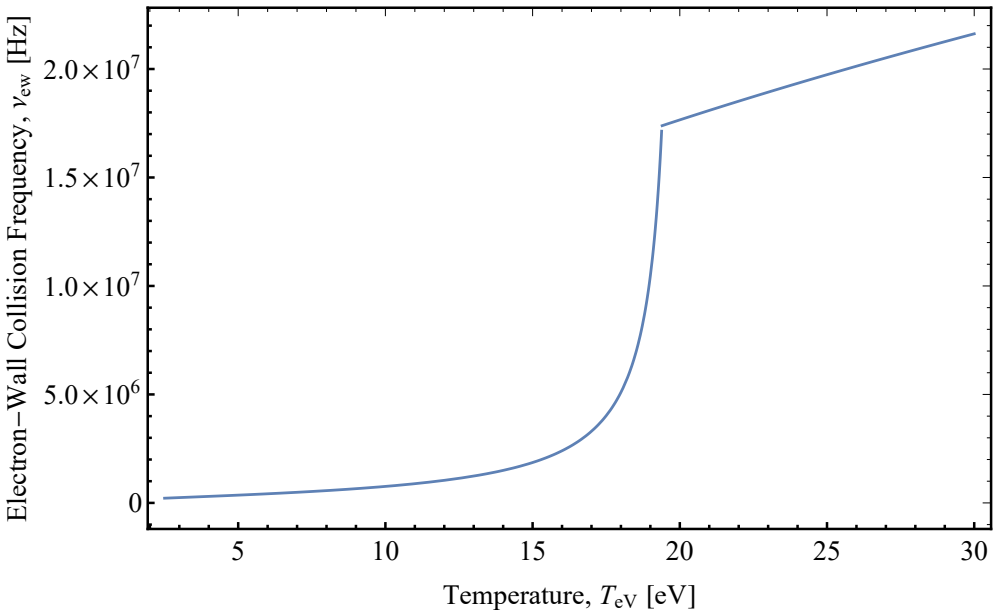

Figure 5.1: Electron-wall collision frequency,ν_{ew}, as a function of localized temperature, T_{eV}, from the minimum to maximum temperature for the system.

As the temperature oscillates in the driven model, so, too, does the time averaged temperature, most notably around the defined acceleration region. Looking at the changing slope in Fig. 5.1, the greatest gains in collision frequency would occur as a region moves from $15eV$ to $20eV$. Given that the maximum of the electric field Gaussian curve is $30eV$, this spike would occur at the very edges of the Gaussian bell.

The collision frequencies achieved in these simulations align well with the assumed frequency used by Hara [18].

5.2 Effects on the Sheath Potential and Mean Electron Energy Loss

Not only does the sheath potential have to contend with the Gaussian effects of the temperature function itself, but this behavior is paired with a natural logarithm, which is also affected by temperature by way of the SEE coefficient, σ. This leads to an unusual function shape, as the Gaussian bell is bisected by another, smaller Gaussian, as shown in Fig. 5.2.

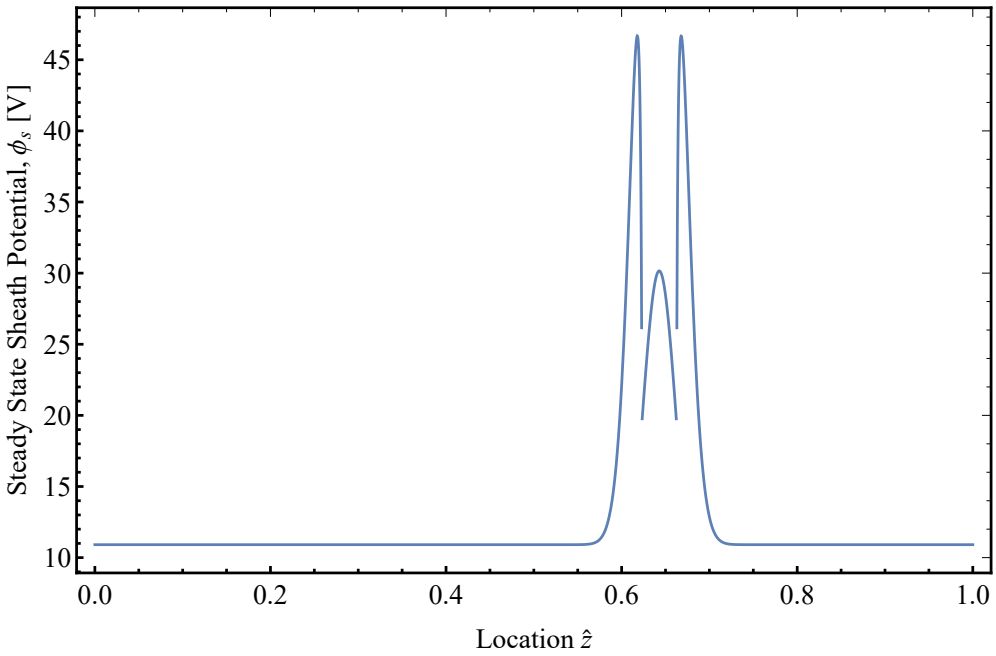

Figure 5.2: Sheath potential of the steady state model, showing a sudden dip around the location of the peak electric field.

Focusing on the region of highest magnitude in the Gaussian, $0.50 \leq \hat{z} \leq 0.75$, the sheath potential oscillates axially in the same manner as the temperature's driven oscillation (Fig. 5.3). Notably, the top sheath potential of approximately $47V$ exists over a wider range of the channel length. Through Eqn. 3.40 this suggests those locations would receive more electrons incoming to the wall as compared to the steady state, and (to add insult to injury), Eqn. 3.42 implies that the electrons would also also lose more mean energy per collision.

As a function of this unusual sheath potential and the localized temperature, the mean electron energy (Fig. 5.4) also exhibits discontinuities in its pseudo-Gaussian curve. From this graph, the maximum energy loss per electron in the thick of the acceleration region can reach roughly 80 V per electron, over four times the minimum energy loss of 20 V.

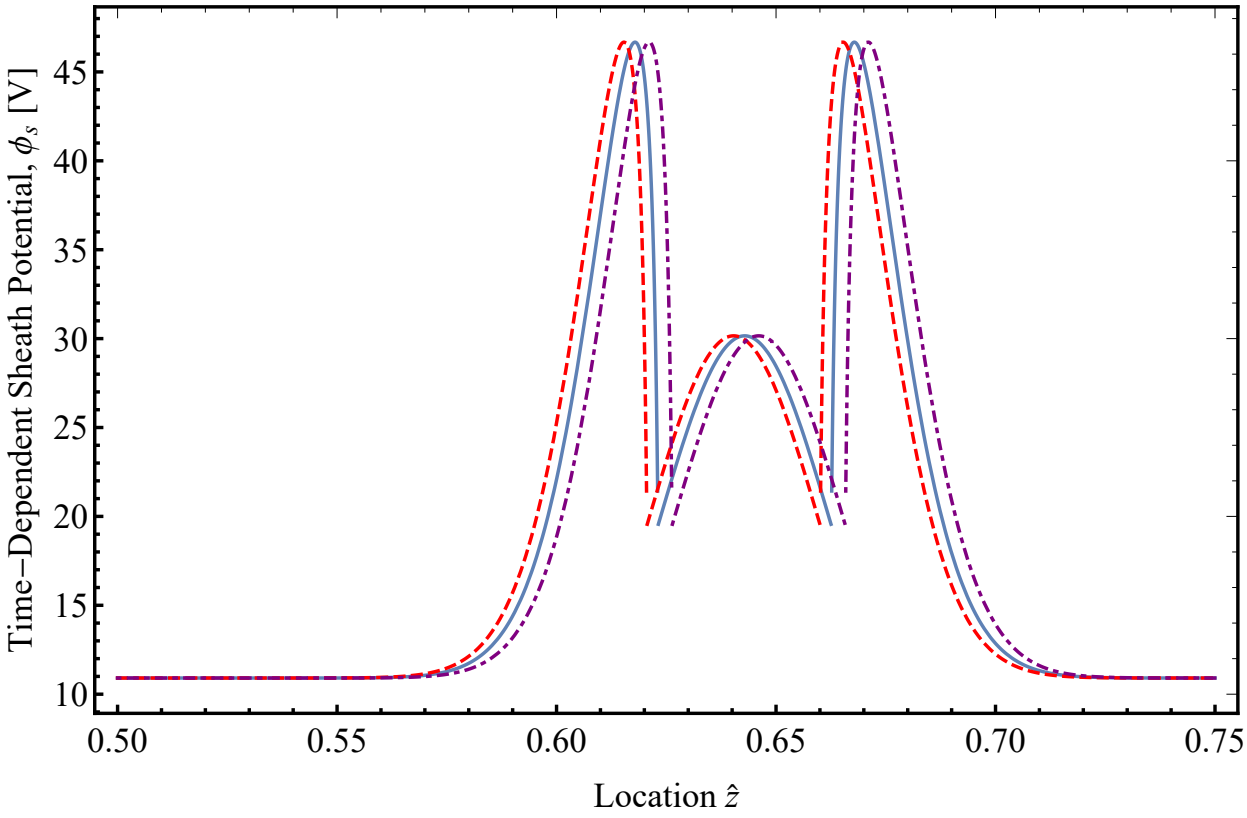

Figure 5.3: Sheath potential near the location of the peak electric field for an oscillation with the nominal linear translation $\hat{z}_s$ and frequency $\hat{\omega}_s$. The blue solid represents the value at the start of the cycle. The red-dashed and purple-dot-dashed lines represent 9 and 16 time steps into the cycle, respectively, to show the range of the function over time.

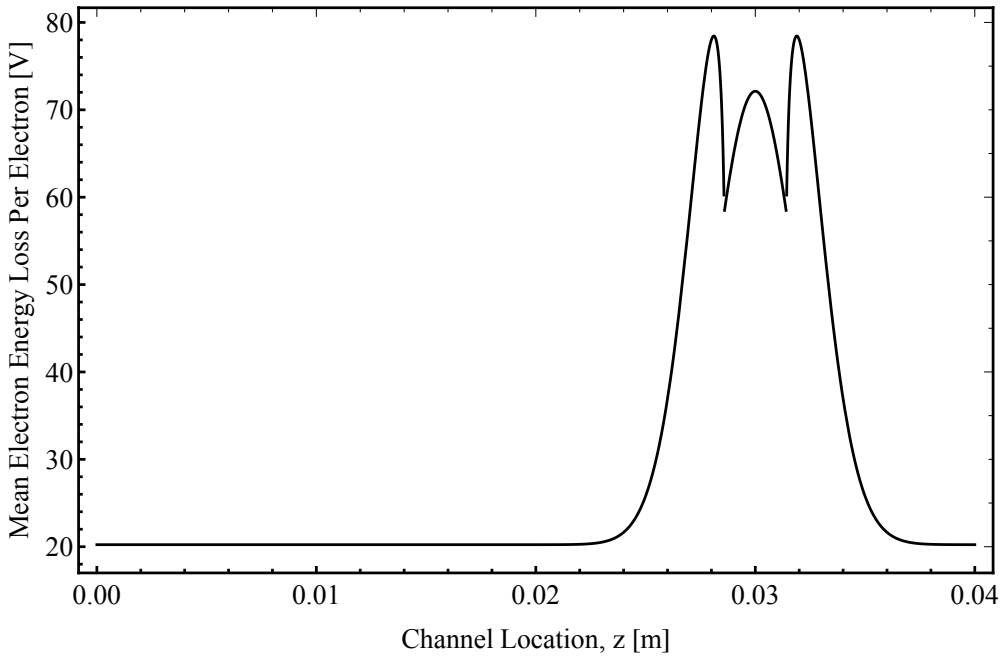

Figure 5.4: Mean electron energy loss as a function of location in the channel, z.

5.3 Localized Flux

In the steady state model, localized flux exhibits two distinct local maximums over the spatial range: one at a location that coincides with maximum plasma density, and another that aligns with maximum electric field. Every time-dependent oscillating model also exhibited this double peak, with the smaller one coming at the same distance before the acceleration region. In both modes, this smaller maximum is a direct result of the peaking plasma density, since the wall loss is proportional to the plasma density according to Eqn. 3.32. This local maximum can be seen in Fig. 5.5. While significant compared to the surrounding magnitudes at over 1500 W/m^2, the maximum value at the peak electric field reaches over 250 kW/m^2; the local maximum is less than one percent of this magnitude.

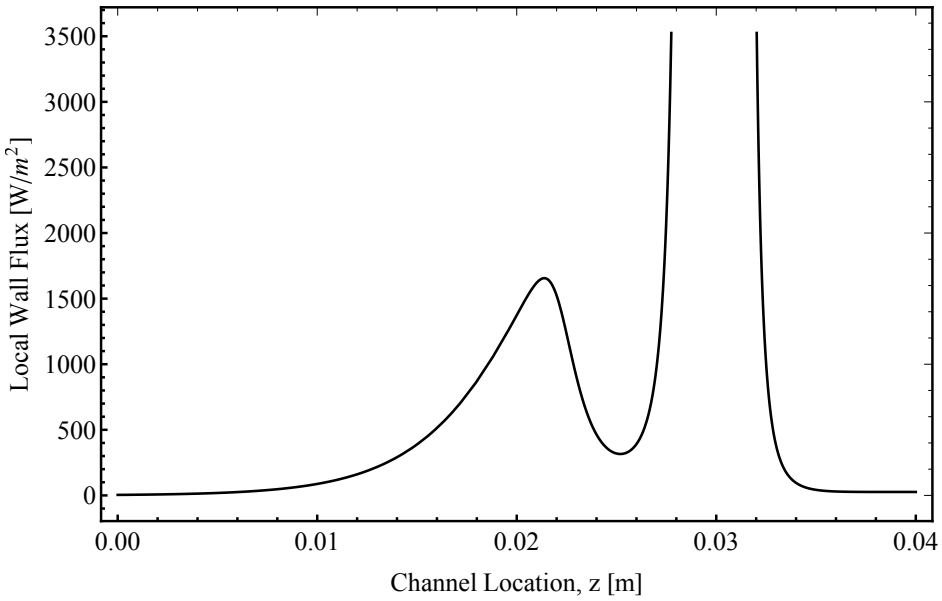

Figure 5.5: The wall flux along the length of the thruster channel. The y-axis is adjusted to highlight the local maximum at approximately 0.02 m, which is upstream of the acceleration region. The maximum value of the wall flux (not shown) is over 250 kW/m^2.

5.4 Power Loss Comparison

For axial displacement case-by-case comparison for power losses to the channel wall, the axial displacement was varied from 0.0001 m to 0.01 m, and the frequency was held at nominal (10 kHz). As seen in Fig. 5.6, the mean value for each of the cases matched the steady state mean value, suggesting that the mean equilibrium value is directly tied to the starting, or central, location of the electric field. The range between the maximum and minimum power magnitudes grows considerably as the displacement distance increases. At the maximum displacement of 0.005 m, the maximum power reaches up to 1634 W, which is greater than the electrical power input into the system (1350 W). However, this is only a momentary spike, much like when the mass utilization peaks above one.

After examining the effects axial displacement has on the quantities, the effects on the power loss are unsurprising: wider movement of the the peak electric field strength can cause

greater spikes in the plasma density, which in turn affect the density of the ions and electrons colliding with the wall. This increases not only the localized heat flux, but the heat flux downstream of that location which will also experience an increased plasma density. The highest power losses here occur when the peak electric field is furthest upstream, such as in the maximum displacement case. Likewise, this case also shows the lowest amount of instantaneous power loss (10 W), likely when the peak electric field is closest to the exit plane.

In contrast to the near-exponential increases by the axial displacement cases, the frequency variation cases show an increase of just over 100 W for peak magnitude across the entirety of the frequency range. The maximum power reaches approximately 500 W, which is 36% of the total input power. Nowhere in this range is there a case where the power loss is more than the input power in, even instantaneously, unlike the axial displacement cases. Likewise, the minimum power loss is only 25% of the total input power, showing that frequency variation does not lead to the same extreme ranges as axial displacement, either.

Goebel estimates that the power losses to the wall in an SPT Hall thruster to abut 50%, though this assumes that the average wall temperature along the entire channel is approximately $25eV$ [16]. The thruster and system studied in this thesis has an average wall temperature of $0.1eV$ due to the Gaussian definition, which could serve to limit the inefficiencies due to the wall losses in the time- and volume-averaged approach Goebel uses and explain why the average power losses are less than a quarter of the input power in this model.

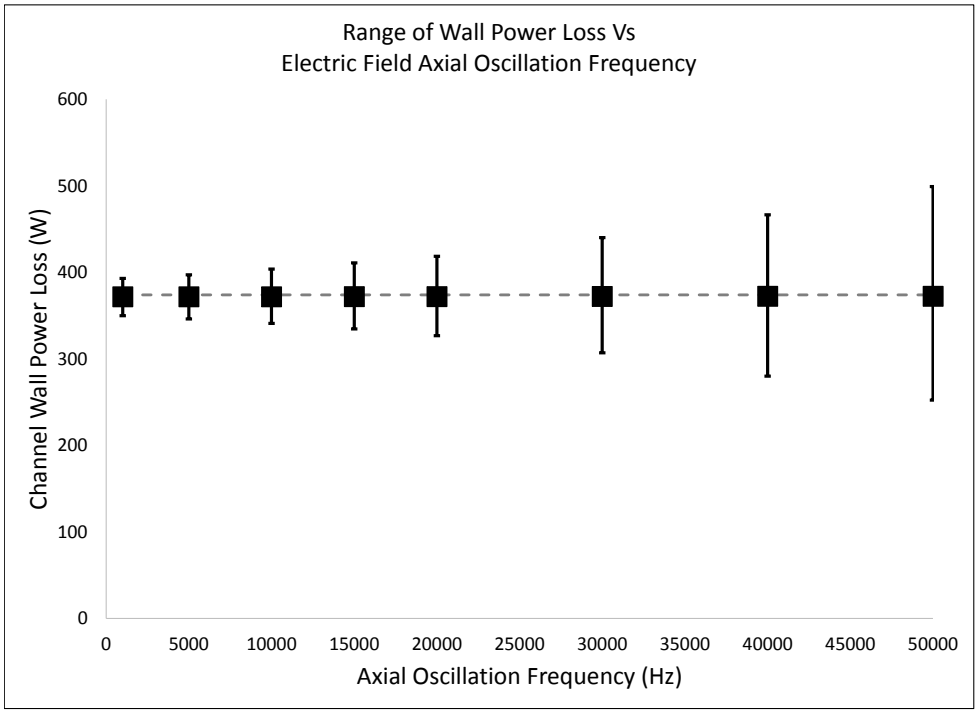

Figure 5.6: Ratio of the linear translation variation, time-dependent power losses to the channel wall versus the steady state power loss.

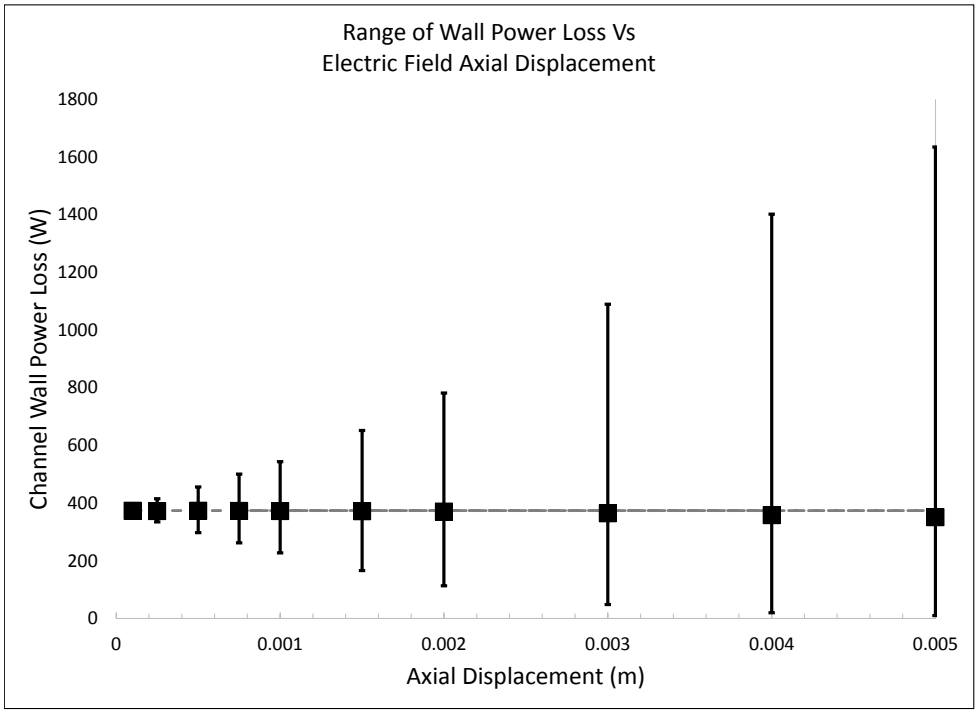

Figure 5.7: Ratio of the frequency variation, time-dependent power losses to the channel wall versus the steady state power loss.

Chapter 6

CONCLUSION

6.1 Thesis Conclusion

6.1.1 Oscillatory Behavior Effects on Plasma Quantities

As discussed in Chapter 4, time dependent oscillations tend to oscillate around the steady state value, albeit not always with symmetrical distributions towards the peaks and troughs. More extreme axial displacements lead to notable irregularities in the sinusoidal signals, especially at the exit plane, while increased frequency does not disrupt the driven oscillations sinusoidal shape. Extreme peaks and troughs occurring at the upstream location also impact the exit plane and can exacerbate values towards either extreme.

Plasma density seems to be particularly sensitive to any change in the steady state: any non-steady electric field causes plasma density to drop in the acceleration region and therefore downstream at the exit plane. As mentioned in Section 4.3, the effective length of the ionization region upstream may be shortening during the oscillations, hampering ionization which results in a lowered density.

Ion velocity, too, appears sensitive to the oscillations; at the exit plane this oscillation can spur nested signals both at start-up and within the stabilized oscillation. Here, the preservation of charge conservation could be the major factor in these irregularities, as its coupled with the electron velocity, which also swings more wildly further downstream. However, which is the cause and which the effect remains elusive; numerically, the use of the ion velocity in the ion momentum equation suggests the ion velocity is the governing quantity.

Since both plasma density and ion velocity are both key to mass utilization, performance of the thruster also oscillates. Instances of a mass utilization over 1 occur, providing another derived quantity to determine breathing mode by.

The oscillation of the flux from the plasma into the wall, and the presence of lag in the neutral density and ion velocity plots, suggests a cyclical feedback system that could induce breathing mode in a system:

1. An initial perturbation of temperature increases the temperature profile over the channel.

2. Since the wall loss into the channel is proportional to temperature, the initial increase leads to an increase in energy flux from the plasma into the channel walls.

3. Increased flux draws more energy from the plasma, causing the average temperature of the plasma to drop.

4. Again, due to the wall loss dependence on temperature, a decrease in plasma temperature leads to decreased flux into the wall.

5. Now, since there is less flux, the temperature starts to rise again.

6. This increase in temperature continues until the wall flux can outpace heat generation in the plasma, and the cycle starts again.

This secondary effects of temperature on plasma density and ion velocity could explain the phase shifting noted by Romadanov, but this would require further study to verify [31].

6.1.2 Oscillatory behavior effects on Power Loss

Likewise, oscillations that "spread" the electric field to a lesser extent would result in power losses closer to the steady state; this can be seen in the smaller axial displacement cases and the frequency cases in general (which do not spread the electric field anymore than the nominal distnace). This behavior of the electric field in the breathing mode has been documented by Young through TR-LIF and is likely valid. [37]

Given the highly non-linear calculations required for some of the terms used to calculate power loss (e.g. sheath potential), fluid models and numerical solvers are essential for understanding the reactions of plasma systems to perturbations. With that said, an incomplete model should be handled with great care so as not to assume too much from the solutions. Power loss reduction, as analyzed in this thesis, is valid if the plasma quantities generated by the models are also valid.

6.2 Next Steps

6.2.1 Avenues for Improved Accuracy

While the ionization rate used in this model is determined from a function that is fitted to tabulated data for $T_{eV} \geq 5\text{eV}$, given that most of the channel lies outside of this temperature range, a more accurate ionization rate could be used. In particular, the BOLSIG+ Boltzmann solver has been used by many other models, Hara included [18]. BOLSIG+ also uses tabulated data to generate coefficients for ionization rates, but using it here for the lower temperature regions could increase the accuracy of the continuity equations of the model [17].

6.2.2 Electron Temperature Inclusion

Including the total energy equation for the electrons could help to stabilize the inherent sensitivities of the electron velocity, and therefore remove the numerical noise that can appear in the time-dependent results. The jagged troughs appearing in the electron velocity (Fig. 4.19) are typical of this numerical deficiency.

Additionally, the model could integrate emerging research about the anode fall phenomenon as described by Dorf et al., where an electron-repelling sheath forms at the anode [12]. This sheath slows electrons at the anode considerably, almost by an entire order of magnitude, which would also affect the boundary conditions for the steady and time-dependent models showcased in this thesis.

6.2.3 Electron Pressure Coupling

Numerically, this model would benefit from additional equations to ensure the system's self-consistency, especially in regards to the electric potential. Towards the conclusion of this thesis, the author attempted to introduce the coupled potential-electron pressure scheme proposed by Hara [20].

Unfortunately, use of this approach changes the system into a differential-algebraic system, which is less amenable to the traditional methods for solving numerical systems (Explicit or Implicit Runge Kutta, BDF, etc). Wolfram's documentation on differential-algebraic systems is extensive and often starts with the suggestion to use the IDA method. Furthermore, by using a second-order equation, the derivatives of the functions used in the pressure coupling scheme need to be well-defined. It is largely due to this computational complexity that this coupling scheme was not pursued in this iteration of the model; viability of the base set of equations needed to be established, first, before this complexity could be added. As seen in these results, remarkable accuracy can still be achieved in the understanding of Hall thruster behavior with a limited number of equations and constraints.

That said, self-consistent model that can show un-driven oscillations in the wall loss term would also be able to support the hypothesis that the oscillating heat flux causes the breathing mode within the channel.

6.2.4 Experimental Notes

This model would benefit from additional integration of experimental results along with new, acceleration-region-focused experimental design. First, anomalous transport terms should be included in order to better align these results with experimental findings, since that is a common gap between the two analyses [4]. Second, rigorous diagnostics to monitor not only the ion density but the electric field of the Hall thruster could inform the accuracy, especially in terms of magnitude. The non-dimensionalization of this model should aid this work, since the absolute geometry of the channel (which often dictates the resources at hand) is of minor

importance.

Experimental data showing the evolution of temperature around the acceleration region with respect to time would also help to illuminate whether cyclical wall losses could be a contributing factor to the breathing mode.

BIBLIOGRAPHY

[1] Serge Barral and Eduardo Ahedo. Low-frequency model of breathing oscillations in hall discharges. *Phys. Rev. E*, 79:046401, Apr 2009.

[2] A.M. Bishaev and Vladimir Kim. Local plasma properties in a hall-current accelerator with an extended acceleration zone. *Zhurnal Tekhnicheskoi Fiziki*, 48:1853–1857, 08 1978.

[3] J. P. Boeuf and L. Garrigues. Low frequency oscillations in a stationary plasma thruster. *Journal of Applied Physics*, 84(7):3541–3554, 1998.

[4] Jean-Pierre Boeuf. Tutorial: Physics and modeling of hall thrusters. *Journal of Applied Physics*, 121(1):011101, 2017.

[5] Vernon H Chaplin, Benjamin A Jorns, Alejandro Lopez Ortega, Ioannis G Mikellides, Ryan W Conversano, Robert B Lobbia, and Richard R Hofer. Laser-induced fluorescence measurements of acceleration zone scaling in the 12.5 kW HERMeS Hall thruster. *Journal of Applied Physics*, 124(18):183302, nov 2018.

[6] E. Y. Choueiri. Plasma oscillations in Hall thrusters. *Physics of Plasmas*, 8(4):1411, mar 2001.

[7] E. Y. Choueiri. A Critical History of Electric Propulsion: The First 50 Years (1906-1956). *Journal of Propulsion and Power*, 20(2):193–203, 2008.

[8] Ryan W. Conversano, Dan M. Goebel, Ioannis G. Mikellides, Richard R. Hofer, and Richard E. Wirz. Performance analysis of a low-power magnetically shielded hall thruster: Computational modeling. *Journal of Propulsion and Power*, 33(4):992–1001, 2017.

[9] Sarah E. Cusson, Ethan T. Dale, Benjamin A. Jorns, and Alec D. Gallimore. Acceleration region dynamics in a magnetically shielded Hall thruster. *Physics of Plasmas*, 26(2), 2019.

[10] Ethan T Dale, Benjamin Jorns, and Kentaro Hara. Numerical investigation of the stability criteria for the breathing mode in Hall Effect Thrusters. Technical report.

[11] Ethan T. Dale and Benjamin A. Jorns. Non-invasive time-resolved measurements of anomalous collision frequency in a Hall thruster. *Physics of Plasmas*, 26(1):013516, jan 2019.

[12] Leonid Dorf, Yevgeny Raitses, Artem Smirnov, and Nathaniel Fisch. Anode Fall Formation in a Hall Thruster. (July):1–7, 2012.

[13] John Fife, Manuel Martinez-Sanchez, and James Szabo. A numerical study of low-frequency discharge oscillations in Hall thrusters. In *33rd Joint Propulsion Conference and Exhibit*, Reston, Virigina, jul 1997. American Institute of Aeronautics and Astronautics.

[14] D Gawron, S Mazouffre, N Sadeghi, and A Héron. Influence of magnetic field and discharge voltage on the acceleration layer features in a Hall effect thruster. *Plasma Sources Science and Technology*, 17(2):025001, may 2008.

[15] Stephen Robert Gildea. *Development of the Plasma Thruster Particle-in-Cell Simulator to Complement Empirical Studies of a Low-Power Cusped-Field Thruster*. PhD thesis, MIT, 2012.

[16] Dan M. Goebel, Ira Katz, and Wiley InterScience (Online service). *Fundamentals of electric propulsion : ion and Hall thrusters*. Wiley, 2008.

[17] G J M Hagelaar and L C Pitchford. Solving the Boltzmann equation to obtain electron transport coefficients and rate coefficients for fluid models. *Plasma Sources Science and Technology*, 14(4):722–733, nov 2005.

[18] Kentaro Hara. Non-oscillatory quasineutral fluid model of cross-field discharge plasmas. *Physics of Plasmas*, 25(12), 2018.

[19] Kentaro Hara. An overview of discharge plasma modeling for Hall effect thrusters. *Plasma Sources Science and Technology*, 28:44001, 2019.

[20] Kentaro Hara and Ioannis G. Mikellides. Characterization of low frequency ionization oscillations in Hall thrusters using a one-dimensional fluid model. *2018 Joint Propulsion Conference*, pages 1–15, 2018.

[21] Kentaro Hara, Michael J. Sekerak, Iain D. Boyd, and Alec D. Gallimore. Perturbation analysis of ionization oscillations in Hall effect thrusters. *Physics of Plasmas*, 21(12), 2014.

[22] W.A. Hargus, Jr. and M.A. Cappelli. Laser-induced fluorescence measurements of velocity within a hall discharge. *Applied Physics B*, 72(8):961–969, Jun 2001.

[23] Kelly Heidman. NASA Profile: Dr. Harold R. Kaufman, Sep 2016.

[24] Ewan Samuel Kay. Numerical models of Hall thruster ionization oscillations. 2016.

[25] Vladimir Kim, Kn Kozubsky, Vjacheslav M Murashko, and Av Semenkin. History of the Hall Thrusters Development in USSR. *30th International Electric Propulsion Conference*, pages 17–20, 2007.

[26] Stephane Mazouffre, Damien Gawron, Vladimir Kulaev, and Nader Sadeghi. Xe+ ion transport in the crossed-field discharge of a 5-kw-class hall effect thruster. *IEEE Transactions on Plasma Science*, (5):1967–1976, oct.

[27] Jeffrey A Mockelman. *Semi-Analytical Model of Ionization Oscillations in Hall Thrusters*. PhD thesis, MIT, 2015.

[28] A. I. Morozov. The conceptual development of stationary plasma thrusters. *Plasma Physics Reports*, 29(3):235–250, mar 2003.

[29] Michael R. Nakles, William A. Hargus, Jorge J. Delgado, and Ronald L. Corey. A 205 Hour Krypton Propellant Life Test of the SPT-100 Operating at 2 kW. *33rd International Electric Propulison Conference*, pages 1–21, 2013.

[30] Michael J Patterson and James S Sovey. History of Electric Propulsion at NASA Glenn Research Center: 1956 to Present. 2013.

[31] I Romadanov, Y Raitses, and A Smolyakov. Hall thruster operation with externally driven breathing mode oscillations. *Plasma Sources Science and Technology*, 27(9):094006, sep 2018.

[32] Erich H. Soendker, Sam Hablitzel, Artie Tolentino, Benjamin Welander, May Allen, and Jerry Jackson. Power Processing and Flow Control for a 100kW Hall Thruster System. jul 2018.

[33] G.N. Tilinin. High-frequency plasma waves in a Hall accelerator with an extended acceleration zone. *Soviet Technical Physics*, 2900(206), 1977.

[34] EK Tsiolkovsky. Investigation of universal space by means of reactive devices, 1903.

[35] J Vaudolon, B Khiar, and S Mazouffre. Time evolution of the electric field in a Hall thruster. *Plasma Sources Science and Technology*, 23(2):022002, feb 2014.

[36] Benjamin Welander, Jeff Monheiser, Nicole Meckel, Kristi De Grys, Peter Peterson, Aerojet, and Lockheed Martin. Demonstration of the XR - 12 Hall Current Thruster. *33rd International Electric Propulsion Conference*, pages 1–10, 2013.

[37] C V Young, A Lucca Fabris, N. A. Macdonald-Tenenbaum, W A Hargus, and M A Cappelli. Time-resolved laser-induced fluorescence diagnostics for electric propulsion and their application to breathing mode dynamics. *Plasma Sources Science and Technology*, 27(9):094004, sep 2018.